

NASA Technical Memorandum 86320

(NASA-TM-86320) EFFECTS OF AIRFOIL SHAPE,
THICKNESS, CAMBER, AND ANGLE OF ATTACK ON
CALCULATED TRANSONIC UNSTEADY AIRLOADS
(NASA) 56 p HC A04/MF A01

N85-18957

CSCI 01A

Unclass

G3/02 14316

Effects of Airfoil Shape,
Thickness, Camber, and
Angle of Attack on Calculated
Transonic Unsteady Airloads

John T. Batina

MARCH 1985



NASA

NASA Technical Memorandum 86320

Effects of Airfoil Shape,
Thickness, Camber, and
Angle of Attack on Calculated
Transonic Unsteady Airloads

John T. Batina
Langley Research Center
Hampton, Virginia

NASA

National Aeronautics
and Space Administration

Scientific and Technical
Information Branch

1985

Contents

Summary	1
Introduction	1
Symbols	1
Transonic Code XTRAN2L and Pulse-Transient Technique	2
General Airfoil Description	3
Linear Unsteady Airloads	3
Results for Three Airfoil Shapes	4
Mean Angle of Attack of 0° With No Camber	4
Mean Angle of Attack of 1.0° With No Camber	4
Mean Angle of Attack of 0° With Camber	5
Results for Three Airfoil Thicknesses	6
Mean Angle of Attack of 0° With No Camber	6
Scaled Mean Angle of Attack of 1.0° With No Camber	7
Mean Angle of Attack of 0° With Scaled Camber	7
Comparison of Effects Due to Angle of Attack With Effects Due to Camber	8
Concluding Remarks	9
References	10

PRECEDING PAGE BLANK NOT FILMED

Summary

The effects of airfoil shape, thickness, camber, and mean angle of attack on transonic unsteady airloads were investigated as calculated by the finite-difference computer code XTRAN2L. This code provides a time-marching solution to the nonlinear small-disturbance equation for transonic flow. The harmonic airloads for airfoil plunge and pitch motions were determined by using the pulse-transient method available in XTRAN2L. Shape effects were investigated by examining the pressure distributions, shock locations, and unsteady airloads for three 10-percent-thick airfoils: NACA 0010, NACA 64A010, and parabolic arc. Thickness effects were determined by studying a single airfoil shape with three different thicknesses: NACA 0008, NACA 0010, and NACA 0012. Angle-of-attack and camber effects were studied by including mean angle of attack or by adding a simple parabolic camber distribution to the originally symmetric airfoils. Comparisons of unsteady airloads for different airfoil configurations show similar results caused by variations in airfoil shape, thickness, camber, or mean angle of attack. This study suggests that computer costs can be reduced by limiting the number of transonic unsteady aerodynamic calculations for small changes in airfoil geometry or angle of attack.

Introduction

Considerable research is being conducted presently to develop finite-difference computer codes for calculating transonic unsteady aerodynamics for aeroelastic applications. One such example is the two-dimensional finite-difference code XTRAN2L (Whitlow 1983), which solves the complete nonlinear small-disturbance potential equation for transonic flow. The XTRAN2L code is a general-frequency version of the low-frequency LTRAN2 code of Ballhaus and Goorjian (1977). Houwink and Van der Vooren (1980) extended the range of applicability in the moderate-frequency NLR version called LTRAN2-NLR. The XTRAN2L code was developed by extensively modifying LTRAN2-NLR. For aeroelastic applications, finite-difference calculations can become costly, especially if the flutter analyst is interested in determining aeroelastic characteristics for a wide range of airfoil geometry and mean angle of attack. In order to limit the number of aerodynamic computations, the influence of changes in airfoil geometry and mean angle of attack on transonic unsteady airloads needs to be understood.

Airfoil shape and thickness effects on transonic airloads and flutter were initially studied by Bland and Edwards (1984). Calculations were made using XTRAN2L for two airfoils at Mach numbers from 0.75 to 0.80 in increments of 0.01. A conventional air-

foil, NACA 64A010, and a supercritical airfoil, MBB-A3, were considered. Both airfoils are AGARD standard configurations (Bland 1979). Agreement was found between the harmonic aerodynamic forces of the NACA 64A010 airfoil at $\alpha_o = 1.0^\circ$ and the MBB-A3 airfoil at $\alpha_o = -0.5^\circ$. The agreement in forces occurred with a Mach number shift of 0.01 and held true for the entire Mach number range considered. This observation suggests that similarities exist in transonic unsteady forces for airfoils of different shape or thickness at different Mach numbers or angles of attack.

The purpose of this research study is to systematically examine in detail the effects of airfoil shape, thickness, camber, and mean angle of attack on transonic unsteady airloads. Transonic aerodynamic calculations were performed using XTRAN2L. Shape effects were investigated by examining the pressure distributions, shock locations, and unsteady airloads for three 10-percent-thick airfoils: NACA 0010, NACA 64A010, and parabolic arc. The Mach numbers considered were $M = 0.76, 0.78, \text{ and } 0.80$. Thickness effects were investigated by considering one airfoil with three different thicknesses: NACA 0008, NACA 0010, and NACA 0012. Mach numbers for the NACA 0010 airfoil were $M = 0.76, 0.78, \text{ and } 0.80$. For the other two airfoils, the Mach number values were selected using the steady transonic similarity relationship of Liepmann and Roshko (1957). The NACA 0010 airfoil was used as the reference in the similarity relationship. Angle-of-attack effects were studied by including mean angle of attack in the XTRAN2L calculations. Camber effects were examined by adding a simple parabolic camber distribution to the originally symmetric airfoils.

Symbols

b	airfoil semichord, $c/2$
c	airfoil chord
c_{l_h}	lift coefficient due to plunge
c_{l_α}	lift coefficient due to pitch, rad^{-1}
c_{m_h}	pitching-moment coefficient about quarter-chord due to plunge
c_{m_α}	pitching-moment coefficient about quarter-chord due to pitch, rad^{-1}
C_p	pressure coefficient
C_p^*	critical pressure coefficient
\bar{C}_p	scaled pressure coefficient (eq. (8))
d	maximum camber height, nondimensionalized by chord

d_o	value of d required to match upper-surface steady shock location to that using 1.0° mean angle of attack
\bar{d}	scaled maximum camber height (eq. (7))
h	plunge displacement in semichords
k	reduced frequency, $\omega b/U$
M	free-stream Mach number
M_{0010}	free-stream Mach number for NACA 0010 airfoil
M_1, M_2, M_3	free-stream Mach numbers for study of thickness effects
S	airfoil shape
t	time
U	free-stream velocity
x	streamwise coordinate relative to leading edge
z	coordinate normal to free stream, positive up
α	angle of attack, deg
α_o	mean angle of attack, deg
$\bar{\alpha}_o$	scaled mean angle of attack (eq. (6))
γ	ratio of specific heats
δ	maximum thickness-to-chord ratio
δ_{0010}	maximum thickness-to-chord ratio for NACA 0010 airfoil
τ	nondimensional time, Ut/b
$\Delta\tau$	size of nondimensional time step
χ	steady transonic similarity parameter (eq. (4))
χ_1, χ_2, χ_3	steady transonic similarity parameters for study of thickness effects
ω	oscillation frequency, rad/sec

Transonic Code XTRAN2L and Pulse-Transient Technique

The original LTRAN2 code (Ballhaus and Goorjian 1977) was developed to time-accurately integrate the low-frequency transonic small-disturbance (TSD) equation with steady-state airfoil and wake boundary conditions. Houwink and Van der Vooren (1980) improved

the algorithm by adding the time-derivative terms to the airfoil and wake boundary conditions. The resulting code was termed LTRAN2-NLR. The XTRAN2L code (Whitlow 1983), developed at NASA Langley Research Center, is an extensive modification of LTRAN2-NLR that solves the complete TSD equation and includes monotone differencing, nonreflecting far-field boundary conditions, an improved grid, and a pulse-transient capability. Details of the XTRAN2L algorithm development and modifications are given by Whitlow (1983). Details of the grid development and pulse capability are given by Seidel, Bennett, and Whitlow (1983). All results of the present study were obtained using the time-marching finite-difference computer code XTRAN2L.

In the present study, pressure distributions and generalized aerodynamic forces are computed for two modes of airfoil motion: vertical translation (plunge) and pitch about the quarter-chord. Typically, unsteady aerodynamic forces are determined by calculating several cycles of forced harmonic oscillation with the last cycle providing the estimate of the forces. Alternatively, harmonic forces may be obtained indirectly from the response due to a step change in a given mode of motion via the Duhamel integral (Ballhaus and Goorjian 1978). Although more economical, the step response method leads to small errors resulting from the numerical approximation of the starting downwash (Seidel, Bennett, and Whitlow 1983). These errors are minimized in the present calculations by using a smoothly varying exponentially shaped pulse (Seidel, Bennett, and Whitlow 1983). For pitch motion, the input pulse is given by

$$\alpha = \alpha_o + 0.5e^{-0.25(\tau-17.5\Delta\tau)^2} \quad (1)$$

and for plunge motion, the input pulse is given by

$$h = 0.02e^{-0.25(\tau-17.5\Delta\tau)^2} \quad (2)$$

where $\Delta\tau$ is the nondimensional time step. The harmonic response is obtained by dividing the Fourier transform of the output force response by that of the input pulse. Use of the pulse-transient technique gives considerable detail in the frequency domain with a significant reduction in cost over the alternative method of calculating multiple harmonic responses. The accuracy of the method for frequencies as high as $k = 2$ was demonstrated by Seidel, Bennett, and Whitlow (1983).

Plunge and pitch pulse-transient calculations were performed using 2048 time steps with $\Delta\tau$ set equal to $5\pi/32$, as done by Bland and Edwards (1984). Spurious oscillations in the lift and moment coefficients determined from the pulse-transient analysis sometimes occur for reduced frequencies $k \leq 0.1$. A typical example for the lift coefficient due to plunge $c_{l,h}$ is shown in figure 1(a) for the NACA 0010 airfoil at $M = 0.78$ and $\alpha_o = 1.0^\circ$. The unsteady results are presented in the

form of real and imaginary coefficients as a function of reduced frequency k . The jagged nature of the curves at low frequencies generally occurs for airfoils with either angle of attack or camber at the higher Mach numbers. In general, these oscillations are more severe for the lift coefficient than for the moment coefficient, and are more severe for the airloads due to plunge than for the airloads due to pitch. These spurious oscillations were traced to cases for which the lift and moment transient responses did not return smoothly to their respective steady-state values. Instead, for large values of τ , they tend to drift about these values with very small amplitudes (approximately two orders of magnitude smaller than the maximum pulse response amplitude). Although this feature of the lift and moment time histories is hardly noticeable, the resulting low-frequency Fourier components are significant. This numerical difficulty was the result of information contained in the latter portion of the time histories and was alleviated by halving the number of time steps. This process also beneficially reduces the total time by a factor of two. Figure 1(b) shows c_{l_h} results for the NACA 0010 airfoil calculated at the same conditions using 1024 time steps. The jagged low-frequency behavior of the c_{l_h} curves has been eliminated, and the pulse-transient computational time has been reduced by one-half.

Results of equal accuracy could be obtained, with an additional computational savings of approximately 50 percent, by using a step-size doubling procedure. In this procedure, the time step size is doubled at times corresponding to quarter intervals of the total time. Time step sizes used are $\Delta\tau = 5\pi/32$, $10\pi/32$, $20\pi/32$, and $40\pi/32$, such that 480 time steps yield a total time that previously required 1024 time steps. Results obtained using step-size doubling for the NACA 0010 airfoil are shown in figure 1(c) and compare almost identically with the c_{l_h} curves of figure 1(b). Therefore, in this report, pulse calculations for plunge motion were recalculated for lifting cases (nonzero mean angle of attack or camber) using step-size doubling and 480 time steps to alleviate the low-frequency spurious effects. No further effort was expended to optimize the procedure. Although the step-size doubling procedure works equally well for pitch motion, the pitch pulse results were not recalculated, because the oscillations at low values of k were generally not as severe in comparison with the plunge pulse results.

General Airfoil Description

The airfoil surface may be expressed as

$$\frac{z}{c} = \delta f\left(\frac{x}{c}\right) = \delta \left[\pm S\left(\frac{x}{c}\right) + 4\frac{d}{\delta}\left(\frac{x}{c}\right)\left(1 - \frac{x}{c}\right) + \frac{\pi}{180}\left(\frac{\alpha_o}{\delta}\right)\left(0.25 - \frac{x}{c}\right) \right] \quad (3)$$

In equation (3), the first term describes the airfoil shape, the second term defines a simple parabolic camber line, and the third term represents the contribution due to mean angle of attack about a quarter-chord pitch axis. Airfoils described by the same function $f(x/c)$ in equation (3) have similar steady flow fields when

$$\chi = \frac{1 - M^2}{[\delta(\gamma^* + 1)M^2]^{2/3}} = \text{Constant} \quad (4)$$

where χ is the steady transonic similarity parameter (Liepmann and Roshko 1957) and $\gamma^* = 2 - (2 - \gamma)M^2$. For a given value of χ , the steady pressure distributions are identical when scaled according to Liepmann and Roshko (1957) as follows:

$$\frac{C_p [(\gamma^* + 1)M^2]^{1/3}}{\delta^{2/3}} = \text{Constant} \quad (5)$$

It is clear from equation (3) that shape, camber, and mean angle of attack may be varied independently. To maintain steady transonic similarity, however, these variations must be done such that $f(x/c)$ is the same function.

Shape effects were investigated by examining three airfoils of constant δ but different shape $S(x/c)$. Thickness effects were studied by assuming a shape $S(x/c)$, considering three different maximum thickness-to-chord ratios δ , and adjusting α_o/δ or d/δ such that $f(x/c)$ is the same function. In both the shape and thickness studies, effects due to mean angle of attack as well as camber were independently investigated.

Linear Unsteady Airloads

In this section, linear unsteady airloads are presented for reference and for comparison with the transonic airloads which follow. The lift coefficient due to plunge c_{l_h} , the pitching-moment coefficient due to plunge c_{m_h} , the lift coefficient due to pitch c_{l_a} , and the pitching-moment coefficient due to pitch c_{m_a} are shown in figures 2(a), 2(b), 2(c), and 2(d), respectively. These results were computed using linear subsonic aerodynamic theory at $M = 0.80$ (Bland 1982). All four aerodynamic coefficients are smooth functions of reduced frequency k . Of particular interest are the moment coefficients. For the pitching-moment coefficient due to plunge c_{m_h} (fig. 2(b)), the real part is a monotonically increasing function of k which is always positive; the imaginary part is a monotonically decreasing function of k . For the pitching-moment coefficient due to pitch c_{m_a} (fig. 2(d)), the real and imaginary parts are zero at $k = 0$, because the moments are calculated about the quarter-chord (aerodynamic center). Both parts are always positive and increase monotonically with reduced frequency.

Results for Three Airfoil Shapes

Shape effects were investigated by using three different symmetric airfoils, each with a 10-percent maximum thickness-to-chord ratio ($\delta = 0.10$). These three airfoil configurations, known as NACA 0010, NACA 64A010, and parabolic arc, are shown in figure 3. The NACA 0010 airfoil is defined by equation (6.2) of Abbott and Von Doenhoff (1959). Airfoil coordinates for the NACA 64A010 airfoil were taken from the table on page 356 of Abbott and Von Doenhoff (1959). For a better definition of the NACA 64A010 airfoil nose, three additional points on the upper and lower surfaces have been included by fitting an ellipse with the correct leading-edge radius to the leading edge and first ordinate. The NACA 0010 and NACA 64A010 airfoils are very similar in shape (fig. 3), but the NACA 0010 airfoil is slightly thicker than the NACA 64A010 near the leading edge. The parabolic-arc airfoil has a very different shape with a sharp leading edge compared with the blunt-nose NACA 0010 and NACA 64A010 airfoils. The maximum thicknesses occur at 30 percent, 40 percent, and 50 percent chord for the NACA 0010, NACA 64A010, and parabolic-arc airfoils, respectively.

In the shape effects study, three cases are considered: (1) Airfoils at a mean angle of attack of 0° with no camber; (2) Airfoils at a mean angle of attack of 1.0° with no camber; and (3) Airfoils at a mean angle of attack of 0° with camber. In case (3), the value assumed for d is 0.00436. Pulse-transient calculations were then performed using XTRAN2L for all three airfoils at $M = 0.76, 0.78,$ and 0.80 . The upper Mach number limit was intentionally restricted in an attempt to avoid the nonunique solutions arising from transonic small-disturbance theory as investigated by Williams, Bland, and Edwards (1984) using XTRAN2L.

Mean Angle of Attack of 0° With No Camber

Steady pressure distributions for the NACA 0010, NACA 64A010, and parabolic-arc airfoils, all at a mean angle of attack of 0° and with no camber, are shown in figure 4(a). At $M = 0.76$, the flow is subcritical for all three airfoils. At $M = 0.78$, small supersonic regions have formed along both the upper and lower airfoil surfaces. At $M = 0.80$, shock waves of moderate strength are present on both surfaces at approximately 37 percent, 51 percent, and 65 percent chord for the NACA 0010, NACA 64A010, and parabolic-arc airfoils, respectively.

Unsteady results for c_{i_h} , c_{m_h} , c_{l_α} , and c_{m_α} are shown in figures 4(b), 4(c), 4(d), and 4(e), respectively. For the lift coefficient due to plunge c_{i_h} in figure 4(b), all three sets of results show similar trends as a function of reduced frequency. The results for the three airfoils are virtually identical for low values of k . At higher

reduced frequencies, $k > 0.3$, the NACA 64A010 curves lie approximately halfway between the NACA 0010 and parabolic-arc curves. For the pitching-moment coefficient due to plunge c_{m_h} in figure 4(c), all three sets of results again show similar trends with frequency. In contrast with the c_{i_h} comparisons of figure 4(b), agreement between the three sets of c_{m_h} results in figure 4(c) is not as good for low values of k . The differences also generally tend to become slightly larger with increasing Mach number. For the lift coefficient due to pitch c_{l_α} (fig. 4(d)), the results for the three airfoils are nearly identical throughout the entire range of reduced frequency plotted. This suggests that c_{l_α} is relatively independent of shape for the three configurations considered. For the pitching-moment coefficient due to pitch c_{m_α} (fig. 4(e)), large differences are observed between the three sets of unsteady curves, which indicates there is a strong dependence upon shape, especially at low k values. The dependence upon shape becomes larger at the higher Mach numbers. For example, the imaginary part of c_{m_α} at $M = 0.80$ for the parabolic-arc airfoil has become negative for $k < 0.12$, which represents a change in the oscillatory moment coefficient from leading to lagging the harmonic pitch motion.

For the three airfoils of different shape at a mean angle of attack of 0° and with no camber, the unsteady airloads show similar trends with frequency, even though the steady pressure distributions and shock locations are very different. Comparing figures 4(b) through 4(e), the lift coefficients show less of an effect due to airfoil shape than the moment coefficients. Differences between unsteady forces, where they exist, are such that the NACA 64A010 forces generally lie approximately halfway between the NACA 0010 and parabolic-arc forces for a given value of k . This observation suggests that the differences in unsteady airloads for these airfoils may be related to differences between airfoil maximum thickness locations or maximum C_p locations rather than to differences in airfoil shape.

Mean Angle of Attack of 1.0° With No Camber

Steady pressure distributions for the NACA 0010, NACA 64A010, and parabolic-arc airfoils all at $\alpha_o = 1.0^\circ$ and with no camber are shown in figure 5(a). At $M = 0.76$, the NACA 0010 airfoil has a supersonic region along the upper surface from approximately 5 percent to 30 percent chord which is terminated by a weak shock wave. The NACA 64A010 and parabolic-arc airfoils have insignificant upper-surface supersonic regions. At $M = 0.78$, there are shock waves on the upper surfaces of all three airfoils. At $M = 0.80$, the shocks are located farther downstream, and both the shock strengths and the size of the supersonic regions are increased. Upper-surface steady shock locations for each of the three airfoils are very different. For the Mach

number range considered, no shocks are present on the lower surfaces of these airfoils with $\alpha_o = 1.0^\circ$.

Unsteady results for c_{l_h} , c_{m_h} , c_{l_a} , and c_{m_a} are shown in figures 5(b), 5(c), 5(d), and 5(e), respectively. As shown in figure 5(b), the c_{l_h} curves for the three airfoils are very similar and almost coincide for $k < 0.3$. For higher values of reduced frequency, the results for the similarly shaped NACA 0010 and NACA 64A010 airfoils agree well, but the parabolic-arc results differ slightly. The agreement may be attributed to closer upper-surface steady shock locations for the NACA 0010 and NACA 64A010 airfoils, which for $M = 0.80$ are at approximately 59 percent and 63 percent chord, respectively. The upper-surface steady shock position for the parabolic-arc airfoil at $M = 0.80$ is near 78 percent chord. As shown in figure 5(c), the c_{m_h} results for the three airfoils are in good general agreement. The curves for the NACA 0010 and NACA 64A010 airfoils again compare better with each other than with those of the parabolic arc, especially as Mach number is increased. The improved agreement at higher Mach numbers may be due to increasingly similar steady shock locations and steady shock strengths for the NACA 0010 and NACA 64A010 airfoils. Note that the real part of c_{m_h} has changed sign for $k \leq 0.3$ at $M = 0.80$. In figure 5(d), small oscillations in c_{l_a} are evident at low k values as previously discussed. The c_{l_a} results for the three airfoils show excellent agreement for $k > 0.1$. In fact, at $M = 0.76$ and $M = 0.78$, the imaginary c_{l_a} curves for the NACA 64A010 and parabolic-arc airfoils coincide. This may be because of weaker steady shocks on the NACA 64A010 and parabolic-arc upper surfaces at $M = 0.76$ and $M = 0.78$ compared with the NACA 0010 airfoil (fig. 5(a)). At $M = 0.80$, the imaginary c_{l_a} curves in figure 5(d) for NACA 0010 and parabolic-arc airfoils coincide; the NACA 64A010 curve has smaller negative values for low reduced frequency. For the Mach numbers considered, the c_{l_a} results shown in figure 5(d) indicate shape independence at higher values of reduced frequency. In figure 5(e), the c_{m_a} curves for the three airfoils show reasonable correlation for $k > 0.3$. For low k values, particularly at $M = 0.80$, the unsteady XTRAN2L results are very dependent upon shape. At $M = 0.78$, the NACA 0010 and NACA 64A010 curves are virtually identical for all values of k . At $M = 0.80$ and $k < 0.1$, the c_{m_a} curves vary in the order of NACA 64A010, NACA 0010, and parabolic arc. Also at $M = 0.80$, the imaginary part of c_{m_a} has changed sign for $k < 0.2$. These high Mach number, low reduced-frequency effects may be attributed to increased shock strengths and to farther-aft shock locations due to nonzero mean angle of attack.

For the three airfoils of different shape at $\alpha_o = 1.0^\circ$ and no camber, the unsteady aerodynamic coefficients show similar trends with reduced frequency. Differences

between the unsteady airloads for the three airfoils at $\alpha_o = 1.0^\circ$ generally vary in the order of NACA 0010, NACA 64A010, and parabolic arc for the coefficients due to plunge (figs. 5(b) and 5(c)). For the coefficients due to pitch (figs. 5(d) and 5(e)), this is not always the case. At $M = 0.80$ for example, the imaginary c_{l_a} curves at low values of k for the NACA 0010 and parabolic-arc airfoils are nearly the same, and the NACA 64A010 values are no longer between these values. At higher Mach numbers, the reversal in the order of the results may be attributed to shock-associated phenomena produced by including mean angle of attack. A comparison of unsteady airloads with $\alpha_o = 0^\circ$ and $\alpha_o = 1.0^\circ$ (figs. 4 and 5, respectively) shows that the effect of mean angle of attack is greatest at the higher Mach numbers. Mean angle of attack also generally affects the moment coefficients more than the lift coefficients and affects the airloads due to pitch more than the airloads due to plunge.

Mean Angle of Attack of 0° With Camber

Steady pressure distributions for the NACA 0010, NACA 64A010, and parabolic-arc airfoils at $\alpha_o = 0^\circ$ and $d = 0.00436$ are shown in figure 6(a). Supersonic regions are present along the upper surfaces of all three airfoils. These supersonic regions increase in size as the Mach number is increased and terminate with strong shock waves. Steady shock locations for the three airfoils are quite different. At $M = 0.80$, small supersonic regions occur on the lower surfaces of the NACA 0010 and NACA 64A010 airfoils.

Unsteady results for the NACA 0010, NACA 64A010, and parabolic-arc airfoils at $\alpha_o = 0^\circ$ and with camber are given in figures 6(b) through 6(e). As shown in figure 6(b), comparison of the c_{l_h} curves for the three airfoils indicates a small effect of shape at higher reduced frequencies. Differences between the unsteady forces for the three airfoils occur in the same order as the variation in airfoil maximum thickness location. At low k values, the c_{l_h} curves are nearly indistinguishable. As shown in figure 6(c), small differences exist between the c_{m_h} coefficients which vary in a fashion similar to the variation of results in figure 6(b). At $M = 0.80$, sign changes have occurred in the real part of c_{m_h} for low reduced frequencies, similar to the $\alpha_o = 1.0^\circ$ and no camber results shown in figure 5(c). The c_{l_a} coefficients for the three airfoils (fig. 6(d)) are essentially the same, except for the parabolic-arc airfoil at $M = 0.80$ and low k values. The NACA 64A010 c_{m_a} curves are approximately halfway between the NACA 0010 and parabolic-arc curves (fig. 6(e)). At $M = 0.78$, and especially at $M = 0.80$, the parabolic-arc results deviate from this spacing for low k values. This deviation may be attributed to a transonic effect of increased upper-

surface shock strengths and to farther-aft shock locations caused by including camber.

For the three airfoils of different shape at $\alpha_o = 0^\circ$ and with a maximum camber height of 0.00436, the unsteady aerodynamic coefficients show similar characteristics as a function of frequency. Differences between unsteady airloads for the three airfoils vary smoothly and may be attributed to differences in maximum thickness location rather than airfoil shape. This may also be attributed to differences in maximum pressure locations or steady shock strengths for the three airfoils. A comparison of unsteady airloads at $\alpha_o = 0^\circ$ with no camber and with $d = 0.00436$ (figs. 4 and 6, respectively) shows that the effect of mean camber is small at $M = 0.76$ and 0.78 , and is larger at $M = 0.80$. This can probably be attributed to increased upper-surface transonic effects produced by adding the parabolic camber line to the originally symmetric airfoils. As with the mean angle of attack, camber also generally affects the moment coefficients more than the lift coefficients and the airloads due to pitch more than the airloads due to plunge.

In the shape effects study, unsteady forces for the NACA 64A010 airfoil generally lie between the NACA 0010 and parabolic-arc unsteady forces. Differences in transonic unsteady airloads for these airfoils may be related to airfoil maximum thickness location or maximum steady pressure location. The lift coefficients show less of an effect due to airfoil shape than the moment coefficients. Mean angle of attack or camber generally affects the moment coefficients more than the lift coefficients and the airloads due to pitch more than the airloads due to plunge. Also, comparison of the unsteady airloads (figs. 4 through 6) shows that the effects due to mean angle of attack are similar to the effects due to camber. This is shown, for example, by comparing the $M = 0.80$ low reduced-frequency c_{m_α} curves of figures 4(e), 5(e), and 6(e).

Results for Three Airfoil Thicknesses

Thickness effects were investigated by considering three symmetric airfoils of the same shape but with different maximum thickness-to-chord ratios. All three airfoils are defined by the shape expression, equation (6.2) of Abbott and Von Doenhoff (1959), with a maximum thickness-to-chord ratio δ of 0.08, 0.10, or 0.12 for the NACA 0008, NACA 0010, or NACA 0012 airfoils, respectively. These airfoil configurations are shown in figure 7. The study of the effects due to airfoil thickness was undertaken to investigate the agreement in unsteady airloads for the NACA 64A010 and MBB-A3 airfoils (Bland and Edwards 1983) at slightly different Mach numbers. These two airfoils have very similar shapes ($S(x/c)$) and differ primarily in thickness and camber. Therefore, it is of interest to investigate,

for a family of airfoils of different thickness, similarities in unsteady airloads at Mach numbers which produce similar steady transonic flow fields.

Figure 8 shows the steady transonic similarity parameter χ as a function of Mach number for the three maximum thickness-to-chord ratios considered. Values for χ are determined for $\delta = 0.10$ at $M = 0.76, 0.78,$ and 0.80 as listed in table 1. Also tabulated are the Mach numbers $M_1, M_2,$ and M_3 for $\delta = 0.08$ and $\delta = 0.12$ computed iteratively using equation (4). Three cases are considered for investigation of the effects of thickness, angle of attack, and camber as in the shape effects study. In each case, conditions are chosen such that the scaled steady pressure distributions on the three airfoils are identical. Values for mean angle of attack α_o and maximum camber height d used in the thickness effects study are listed in table 2. The values selected for mean angle of attack α_o result in a constant scaled mean angle of attack defined by

$$\bar{\alpha}_o = \alpha_o \left(\frac{\delta_{0010}}{\delta} \right) \quad (6)$$

The values selected for maximum camber height d result in a constant scaled maximum camber height defined by

$$\bar{d} = d \left(\frac{\delta_{0010}}{\delta} \right) \quad (7)$$

Mean Angle of Attack of 0° With No Camber

Steady pressure distributions for the NACA 0008, NACA 0010, and NACA 0012 airfoils, all at $\alpha_o = 0^\circ$ and with no camber, are shown in figure 9(a). The steady pressures are scaled to those of the reference NACA 0010 airfoil. Combining equations (4) and (5) leads to the simple scaling relationship

$$\bar{C}_p = C_p \left(\frac{\delta_{0010}}{\delta} \right) \left(\frac{\sqrt{1-M^2}}{\sqrt{1-M_{0010}^2}} \right) \quad (8)$$

As can be seen in figure 9(a), the scaled steady pressure distributions are identical at each Mach number ($M_1, M_2,$ and M_3).

Unsteady aerodynamic coefficients $c_{l_\alpha}, c_{m_\alpha}, c_{l_\alpha},$ and c_{m_α} as functions of reduced frequency k are plotted in figures 9(b), 9(c), 9(d), and 9(e), respectively. The unsteady aerodynamic coefficients are not scaled, because there are no known unsteady transonic similarity laws. For the lift coefficient due to plunge c_{l_α} shown in figure 9(b), the results for the three airfoils are nearly coincident at low reduced frequencies. At higher reduced frequencies, differences due to thickness are apparent. Here, the c_{l_α} results for the three airfoils of different thickness do not show the consistent variations for a given k value that were found in the shape

effects study at $\alpha_o = 0^\circ$ and with no camber. For the pitching-moment coefficient due to plunge c_{m_h} shown in figure 9(c), the three sets of curves again compare well at low k values. As with the c_{l_h} comparisons of figure 9(b), differences between the three sets of c_{m_h} results occur at higher values of k . For both c_{l_h} and c_{m_h} , these absolute differences are smallest at the highest Mach numbers considered ($M = M_3$). For the lift coefficient due to pitch c_{l_α} shown in figure 9(d), the three sets of curves also indicate differences due to thickness. At $k = 0$, the values for the real part of c_{l_α} are slightly different for the three airfoils, because the steady pressure distributions, and hence lift coefficients, scale differently than angle of attack. (See eqs. (6) and (8).) For the pitching-moment coefficient due to pitch c_{m_α} (fig. 9(e)), the imaginary parts show fairly close agreement for low k values. The real part of c_{m_α} for the three airfoils shows large differences over most of the range of reduced frequency plotted.

For the NACA 0008, NACA 0010, and NACA 0012 airfoils, the unsteady airloads show similar trends with frequency at the Mach numbers investigated. However, differences between the unsteady airloads for the three airfoils of different thickness are apparent, even though the steady flow fields are scaled. The differences may be attributed to variation in maximum thickness or to differences in maximum steady pressure, because the maximum thickness locations and maximum steady pressure locations for the three airfoils are identical. Agreement between unsteady results for these airfoils improves at the higher Mach numbers considered. This is most clearly seen in the moment coefficients (figs. 9(c) and 9(e)), where the absolute differences between the three sets of unsteady airloads decrease and occur at a lower range of reduced frequency with increasing Mach number. These observations suggest that although effects due to thickness are important, effects due to differences in thickness become less important with increasing Mach number.

Scaled Mean Angle of Attack of 1.0° With No Camber

Scaled steady pressure distributions for the NACA 0008, NACA 0010, and NACA 0012 airfoils at a scaled mean angle of attack $\bar{\alpha}_o$ of 1.0° and with no camber are shown in figure 10(a). As before, the scaled steady pressure distributions for the three airfoils are the same for each of the three cases.

Unsteady results for the three airfoils at $\bar{\alpha}_o = 1.0^\circ$ and no camber are shown in figures 10(b) through 10(e). In figure 10(b), the c_{l_h} curves for the NACA 0008, NACA 0010, and NACA 0012 airfoils are in good agreement. In figure 10(c), the c_{m_h} results indicate a small effect due to thickness. As Mach number increases,

the differences between the results for the three airfoils become smaller. For the imaginary part of c_{l_h} (fig. 10(b)) and the real part of c_{m_h} (fig. 10(c)), both at $M = M_1$, the NACA 0010 curves are approximately midway between NACA 0008 and NACA 0012 curves. As Mach number is increased this characteristic deteriorates. In figure 10(d), the c_{l_α} results agree well for the NACA 0008, NACA 0010, and NACA 0012 airfoils. This good agreement, especially at higher Mach numbers, suggests that c_{l_α} is relatively independent of changes in thickness when $\bar{\alpha}_o = 1.0^\circ$. In figure 10(e), the c_{m_α} curves for the lower Mach numbers exhibit the same equally spaced characteristic as in the c_{l_h} and c_{m_h} calculations. Of interest is the large increase with Mach number in the real part of c_{m_α} at $k = 0$. This change is a result of an aft movement of the aerodynamic center produced by increasing Mach number.

For the airfoils of different thickness at $\bar{\alpha}_o = 1.0^\circ$ and no camber, the unsteady forces have similar characteristics as a function of reduced frequency. Differences between the unsteady forces for the NACA 0008, NACA 0010, and NACA 0012 airfoils are apparent even though the steady flow fields were scaled. Overall, the three sets of results are in fairly good agreement. In general, the lift-coefficient results (figs. 10(b) and 10(d)) show better agreement than the moment coefficient results (figs. 10(c) and 10(e)). A comparison of unsteady airloads with and without a scaled mean angle of attack of 1.0° shows that the agreement between the unsteady forces for the NACA 0008, NACA 0010, and NACA 0012 airfoils is improved with the inclusion of scaled mean angle of attack. This is seen clearly, for example, by comparing differences in results for the three airfoils for the pitching-moment coefficient due to pitch c_{m_α} in figures 9(e) and 10(e). The improvement in the agreement between the three sets of transonic unsteady airloads shown in figure 10(e) may be attributed to increased shock strengths and to farther-aft upper-surface shock locations produced by scaled mean angle of attack.

Mean Angle of Attack of 0° With Scaled Camber

Scaled steady pressure distributions for the NACA 0008, NACA 0010, and NACA 0012 airfoils at $\bar{\alpha}_o = 0^\circ$ and with a scaled parabolic camber of 0.00436 added to the originally symmetric profiles are shown in figure 11(a). The scaled steady pressure distributions for the three airfoils are the same for each of the three cases.

Unsteady aerodynamic coefficients for the three airfoils at $\bar{\alpha}_o = 0^\circ$ and with scaled camber are shown in figures 11(b) through 11(e). As shown in figure 11(b), the c_{l_h} curves for the NACA 0008, NACA 0010, and NACA 0012 airfoils with scaled camber agree well, especially at low reduced frequencies. The c_{m_h} results for

the three airfoils also show good agreement at low k values (fig. 11(c)). Generally, absolute differences between the three sets of c_{m_h} curves get smaller as Mach number is increased. As shown in figure 11(d), the c_{l_α} curves indicate some effects caused by differences in thickness at the lower Mach numbers considered. Large differences between the c_{m_α} curves are observed for the three airfoils (fig. 11(e)). This again demonstrates the effects of thickness on the unsteady airloads. The differences become slightly smaller as Mach number is increased. Also, the nonzero value for the real part of c_{m_α} at $M = M_3$ and $k = 0$ is a result of the aft movement of the aerodynamic center.

For the airfoils of different thickness at $\bar{\alpha}_0 = 0^\circ$ and with $\bar{d} = 0.00436$, the unsteady airloads have similar trends with frequency. However, differences between the unsteady forces exist even when the steady pressure distributions are scaled and the steady shock locations are matched. Overall, the unsteady results for the three airfoils are in agreement, although the lift-coefficient results show less of an effect due to changes in thickness than the moment-coefficient results. Agreement between the three sets of results also generally improves as the Mach number is increased. A comparison of unsteady airloads with no camber and with a scaled camber of 0.00436 (figs. 9 and 11, respectively) shows that the agreement between the unsteady forces for the three airfoils is slightly improved with the inclusion of scaled camber.

In the thickness effects study, unsteady forces for the NACA 0008, NACA 0010, and NACA 0012 airfoils show that effects due to differences in thickness become less important with increasing Mach number. The agreement between the unsteady forces for the three airfoils is improved with increasing Mach number, with the inclusion of scaled mean angle of attack, or with the inclusion of scaled camber. Also, comparison of the unsteady airloads of figures 9 through 11 shows that the effects due to scaled mean angle of attack are similar to the effects due to scaled camber. It is anticipated that if the steady shock locations and shock strengths were the same, the transonic unsteady airloads for mean angle of attack and camber might compare even more favorably.

Comparison of Effects Due to Angle of Attack With Effects Due to Camber

Comparisons of unsteady results from both the shape and thickness studies show similarities between effects due to mean angle of attack and camber. In this section, effects due to mean angle of attack and effects due to parabolic camber are directly compared for the NACA 64A010 airfoil at $M = 0.76, 0.78,$ and 0.80 by matching steady shock locations. Angle-of-attack results were computed using $\alpha_0 = 1.0^\circ$. Camber results were computed using values for the maximum camber

height d_0 which match the steady shock locations with those using $\alpha_0 = 1.0^\circ$. In general, values for d_0 are determined by making successive steady XTRAN2L runs and varying the maximum camber height d until the $\alpha_0 = 1.0^\circ$ steady shock locations are matched. For both $M = 0.76$ and $M = 0.78$, the camber height was 0.00436 for the NACA 64A010 airfoil using XTRAN2L. For $M = 0.80$, the camber height is 0.0051.

Steady pressure distributions for the NACA 64A010 airfoil, including either $\alpha_0 = 1.0^\circ$ or $d = d_0$, are shown in figure 12(a). Upper-surface steady shock locations are at approximately 43 percent, 51 percent, and 63 percent chord for $M = 0.76, 0.78,$ and 0.80 , respectively. The two sets of steady pressure results demonstrate that the shock locations are identical and the shock strengths are similar. Also, the pressure curves for the cambered airfoil show more of an aft loading than the pressure curves for the airfoil at mean angle of attack.

Unsteady transonic airloads $c_{l_h}, c_{m_h}, c_{l_\alpha},$ and c_{m_α} for the NACA 64A010 airfoil are shown in figures 12(b), 12(c), 12(d), and 12(e), respectively. For the lift coefficient due to plunge (fig. 12(b)) and the pitching-moment coefficient due to plunge (fig. 12(c)), the $\alpha_0 = 1.0^\circ$ results are nearly identical to the $d = d_0$ camber results for the entire range of reduced frequency plotted. For the lift coefficient due to pitch (fig. 12(d)), the two sets of results agree well. For the pitching-moment coefficient due to pitch (fig. 12(e)), larger differences between the $\alpha_0 = 1.0^\circ$ and $d = d_0$ curves are observed in comparison with the $c_{l_h}, c_{m_h},$ and c_{l_α} results. The largest difference between the c_{m_α} results for the two cases occurs in the imaginary part of c_{m_α} at $M = 0.80$ for $k \leq 0.25$. These differences may be attributed to differences in steady shock strengths.

In general, comparison of the $\alpha_0 = 1.0^\circ$ results with the $d = d_0$ camber results shows good agreement. The agreement is generally better for the coefficients due to plunge (figs. 12(b) and 12(c)) than for the coefficients due to pitch (figs. 12(d) and 12(e)). This good agreement suggests that for the same airfoil shape, combinations of mean angle of attack and camber can result in similar unsteady transonic airloads if the steady shock locations and shock strengths are matched.

The results of this section, as well as results from the shape and thickness studies, help explain the agreement between the harmonic aerodynamic forces of the NACA 64A010 and MBB-A3 airfoils discovered by Bland and Edwards (1984). The agreement in unsteady forces between the NACA 64A010 airfoil at $\alpha_0 = 1.0^\circ$ and the MBB-A3 airfoil at $\alpha_0 = -0.5^\circ$ occurred with a Mach number shift of 0.01, which held true for the entire Mach number range considered, $0.75 \leq M \leq 0.80$. The conventional airfoil used by Bland and Edwards (1984) was the Ames model of the NACA 64A010 airfoil

(Bland 1979). This airfoil differs from the symmetric 10-percent-thick NACA 64A010 airfoil considered here in that it is about 10.6 percent thick and has a very small amount of camber. The MBB-A3 is an 8.9 percent maximum thickness-to-chord airfoil with a supercritical camber distribution. As shown in figure 13, the shape ($S(x/c)$) of the MBB-A3 airfoil (without camber) compares closely with that of the NACA 64A010. Here, the NACA 64A010 airfoil was scaled down 11 percent for direct comparison with the MBB-A3. The shapes are very similar; therefore, the maximum thickness locations are approximately equal. To determine scaled steady flow fields, a Mach number shift is required, because the two airfoils have different maximum thickness-to-chord ratios δ . For the uncambered MBB-A3 airfoil at $M = 0.79$, for example, the steady transonic similarity parameter χ is 1.357. Holding the value for χ fixed to calculate the Mach number corresponding to the similar steady flow field for the NACA 64A010 airfoil gives $M = 0.776$, or a Mach number shift of 0.014. With the inclusion of camber for the MBB-A3 airfoil and mean angle of attack for both airfoils, the Mach number shift may be slightly different in order to match the steady shock location. Actually, for similar steady flow fields, a mean angle of attack of 1.0° for the NACA 64A010 airfoil requires a mean angle of attack of 0.89° for the uncambered MBB-A3 airfoil. For the original MBB-A3 airfoil with positive camber, a mean angle of attack less than 0.89° must be used to produce the same steady shock location. In the study by Bland and Edwards (1984), a mean angle of attack of -0.5° was assumed in all calculations for the MBB-A3 airfoil. Thus, by matching the steady shock locations and strengths for two similar airfoils, the present results show that good agreement between the unsteady transonic airloads can be expected. These results also explain the agreement found by Bland and Edwards (1984).

Concluding Remarks

The effects of airfoil shape, thickness, camber, and mean angle of attack on calculated transonic unsteady airloads were investigated. Shape effects were studied by considering three symmetric airfoils with a 10-percent maximum thickness-to-chord ratio: NACA 0010, NACA 64A010, and parabolic arc. Thickness effects were investigated by considering three symmetric airfoils of the same shape with different maximum thickness-to-chord ratios: NACA 0008, NACA 0010, and NACA 0012. Angle-of-attack and camber effects were studied in both the shape and thickness studies. The harmonic forces for airfoil plunge and pitch motions were computed using the pulse-transient technique of the XTRAN2L transonic small-disturbance code.

The results of this study give an indication of the relative importance of small changes in airfoil configuration. Detailed comparisons of the transonic unsteady airloads as functions of reduced frequency reveal similarities in the results caused by changes in airfoil shape, thickness, camber, or angle of attack. These similarities offer insight into how the number of transonic unsteady aerodynamic calculations might be limited for small changes in airfoil geometry or mean angle of attack. This limitation results in a reduction in computer costs.

At the same Mach number, the three airfoils with different shapes (NACA 0010, NACA 64A010, and parabolic arc) yield transonic unsteady airloads that have similar trends with reduced frequency, even though their steady pressure distributions and shock locations are very different. Differences between unsteady aerodynamic forces, where they exist, are such that the NACA 64A010 forces are generally between the NACA 0010 and parabolic-arc forces for a given value of reduced frequency. The results show that the differences in unsteady airloads for these airfoils are related to airfoil maximum thickness locations, maximum steady pressure locations, or steady shock strengths rather than to differences in airfoil shape.

At Mach numbers determined using steady transonic similarity, the three airfoils of different thickness (NACA 0008, NACA 0010, and NACA 0012) yield transonic unsteady airloads with similar characteristics as functions of reduced frequency. Agreement between steady results for the airfoils of different thickness generally improves at the higher Mach numbers considered. Agreement also improves by including (scaled) mean angle of attack or by adding (scaled) camber to the originally symmetric airfoil shape. The results show that, although effects due to thickness are important, effects due to differences in thickness become less important with increasing shock strength.

In both the shape and thickness studies, similarities between effects due to mean angle of attack and effects due to camber on transonic unsteady forces were found. For the symmetric NACA 64A010 airfoil at a mean angle of attack of 1.0° , the steady shock locations were matched with those of the same airfoil by including camber. The two configurations produced similar steady shock strengths and resulted in transonic unsteady airloads that showed very good agreement. Combinations of mean angle of attack and camber result in similar unsteady airloads if the steady shock locations and shock strengths are the same. The results of this study offer an explanation for the agreement in transonic unsteady airloads between the NACA 64A010 and MBB-A3 airfoils reported by Bland and Edwards (*J. Aircr.*, vol. 21, no. 3, Mar. 1984, pp. 209-217).

NASA Langley Research Center
Hampton, VA 23665
November 14, 1984

References

- Abbott, Ira H.; and Von Doenhoff, Albert E. c.1959: *Theory of Wing Sections*. Dover Publ., Inc.
- Ballhaus, W. F.; and Goorjian, P. M. 1977: Implicit Finite-Difference Computations of Unsteady Transonic Flows About Airfoils. *AIAA J.*, vol. 15, no. 12, Dec., pp. 1728-1735.
- Ballhaus, W. F.; and Goorjian, P. M. 1978: Computation of Unsteady Transonic Flows by the Indicial Method. *AIAA J.*, vol. 16, no. 2, Feb., pp. 117-124.
- Bland, S. R., compiler 1979: *AGARD Two-Dimensional Aeroelastic Configurations*. AGARD AR-156.
- Bland, Samuel R. 1982: *Development of Low-Frequency Kernel-Function Aerodynamics for Comparison With Time-Dependent Finite-Difference Methods*. NASA TM-83283.
- Bland, Samuel R.; and Edwards, John W. 1984: Airfoil Shape and Thickness Effects on Transonic Airloads and Flutter. *J. Aircr.*, vol. 21, no. 3, Mar., pp. 209-217.
- Houwink, R.; and Van der Voren, J. 1980: Improved Version of LTRAN2 for Unsteady Transonic Flow Computations. *AIAA J.*, vol. 18, no. 8, Aug., pp. 1008-1010.
- Liepmann, H. W.; and Roshko, A. c.1957: *Elements of Gasdynamics*, John Wiley & Sons, Inc.
- Seidel, David A.; Bennett, Robert M.; and Whitlow, Woodrow, Jr. 1983: *An Exploratory Study of Finite-Difference Grids for Transonic Unsteady Aerodynamics*. AIAA-83-0503, Jan.
- Whitlow, Woodrow, Jr. 1983: *XTRAN2L: A Program for Solving the General-Frequency Unsteady Transonic Small Disturbance Equation*. NASA TM-85723.
- Williams, M. H.; Bland, S. R.; and Edwards, J. W. 1984: *Flow Instabilities in Transonic Small-Disturbance Theory*. NASA TM-86251.

TABLE 1. MACH NUMBERS FOR NACA 0008, NACA 0010, AND NACA 0012 AIRFOILS
DETERMINED USING STEADY TRANSONIC SIMILARITY

Airfoil	δ	M_1	M_2	M_3
		($\chi_1 = 1.4749$)	($\chi_2 = 1.3270$)	($\chi_3 = 1.1851$)
NACA 0008	0.08	0.7878	0.8060	0.8241
NACA 0010	.10	.76	.78	.80
NACA 0012	.12	.7355	.7569	.7784

TABLE 2. VALUES FOR MEAN ANGLE OF
ATTACK AND MAXIMUM CAMBER HEIGHT
USED IN THICKNESS EFFECTS STUDY

Airfoil	α_o , deg	d
NACA 0008	0.8	0.00349
NACA 0010	1.0	.00436
NACA 0012	1.2	.00524

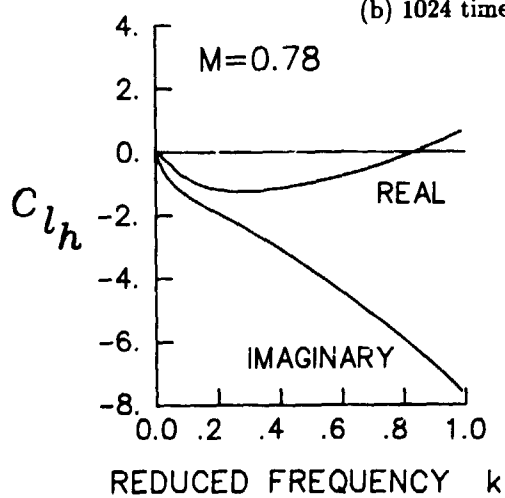
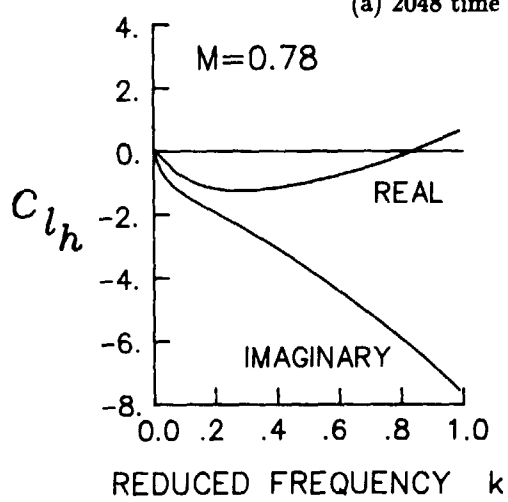
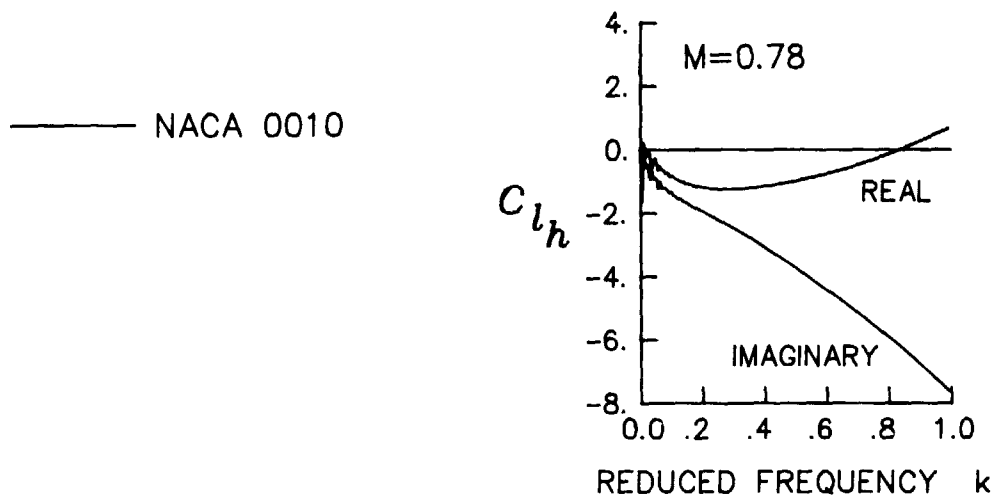
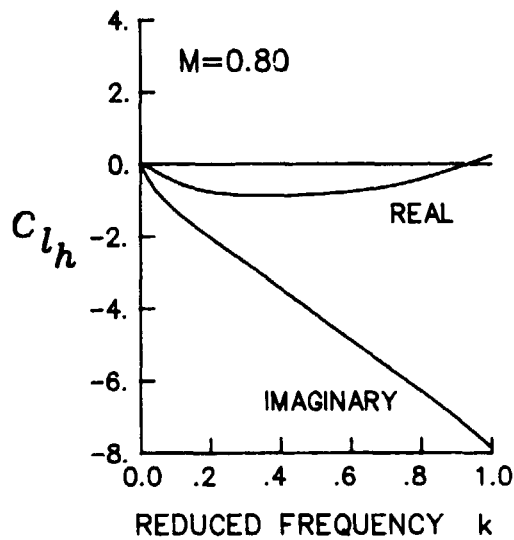
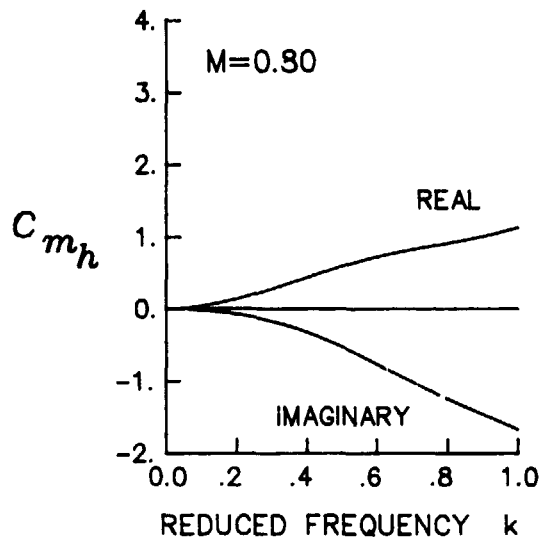


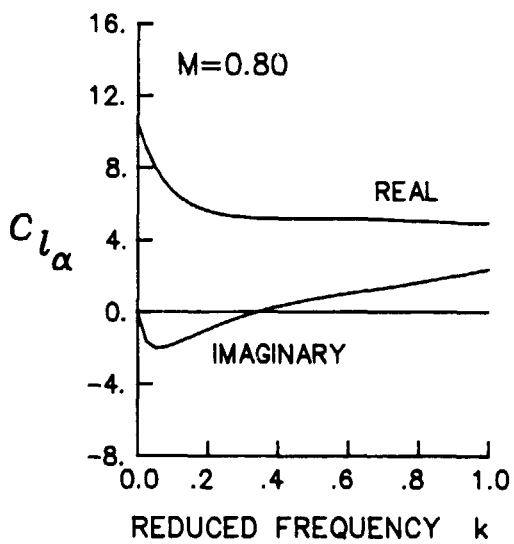
Figure 1. Lift coefficient due to plunge c_{l_h} for NACA 0010 airfoil at $M = 0.78$ and $\alpha_0 = 1.0^\circ$.



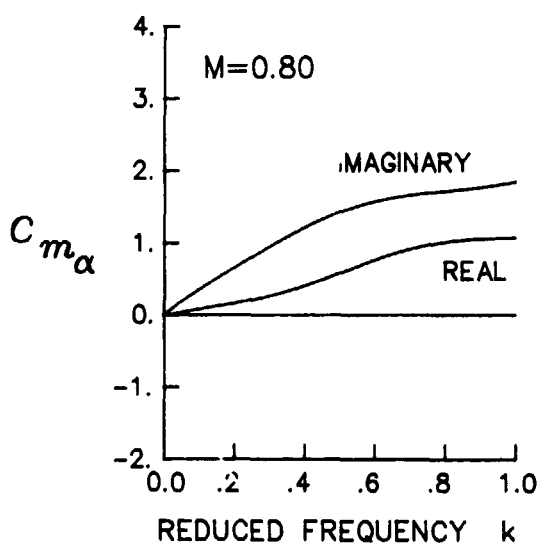
(a) Lift coefficient due to plunge.



(b) Pitching-moment coefficient due to plunge.



(c) Lift coefficient due to pitch.



(d) Pitching-moment coefficient due to pitch.

Figure 2. Unsteady aerodynamic coefficients computed using subsonic linear theory at $M = 0.80$.

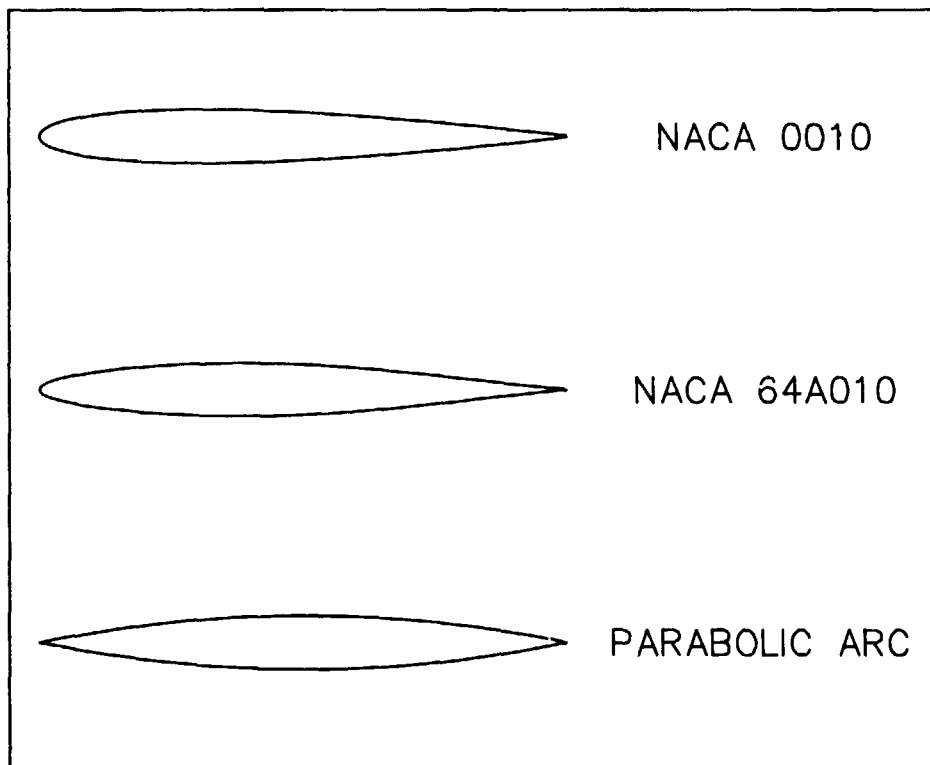
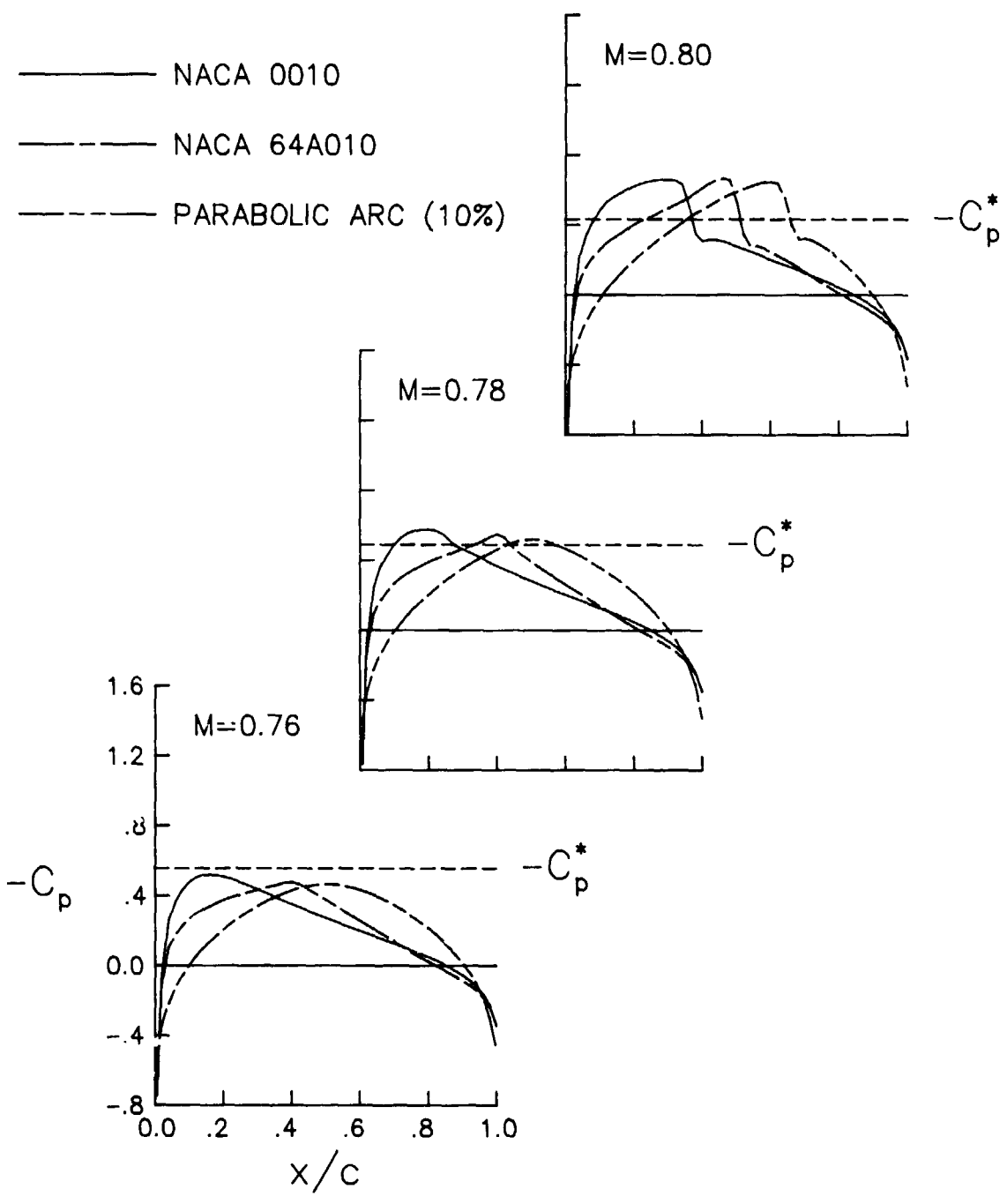
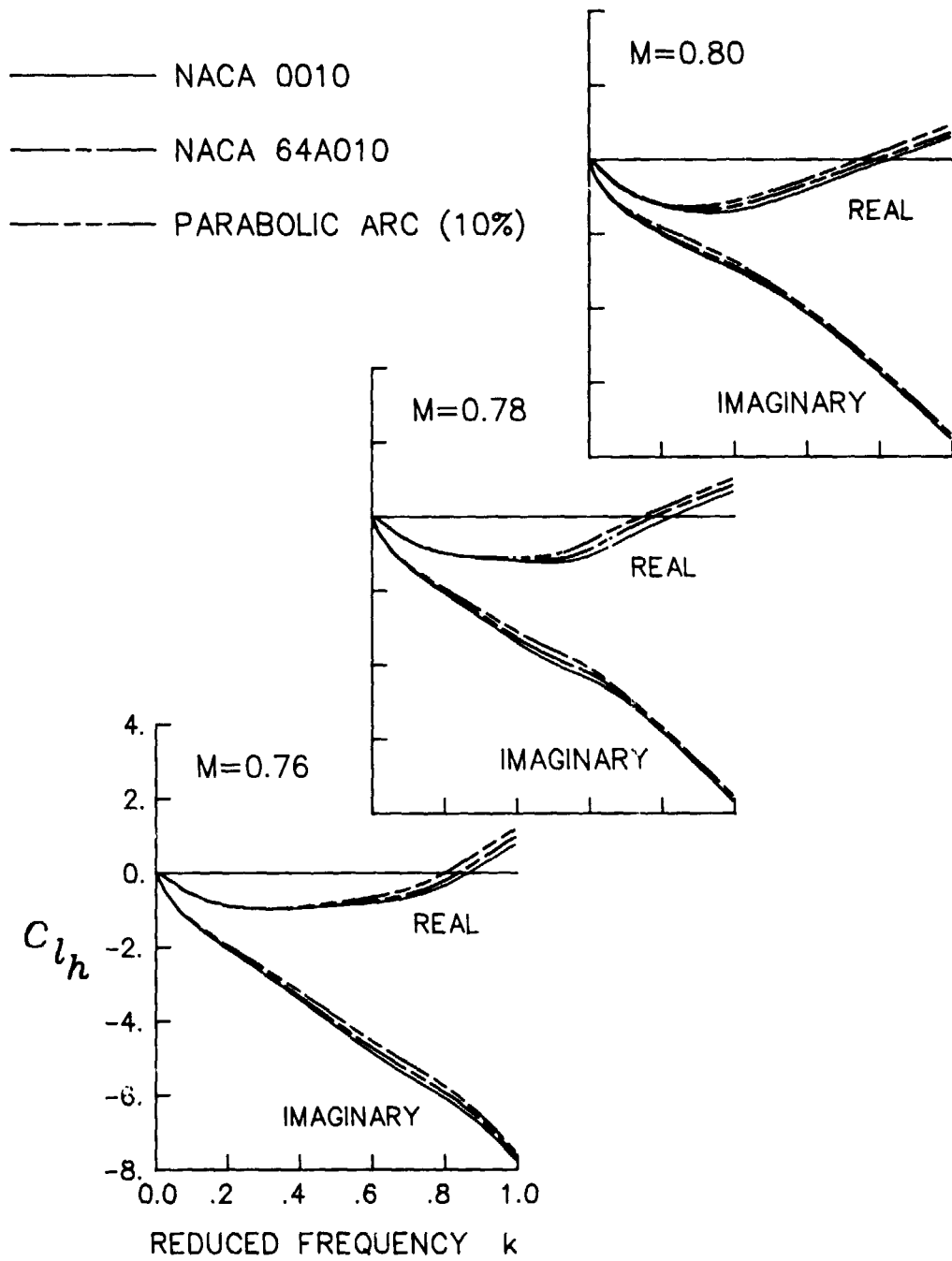


Figure 3. Profiles of NACA 0010, NACA 64A010, and parabolic-arc airfoils used in shape effects study.



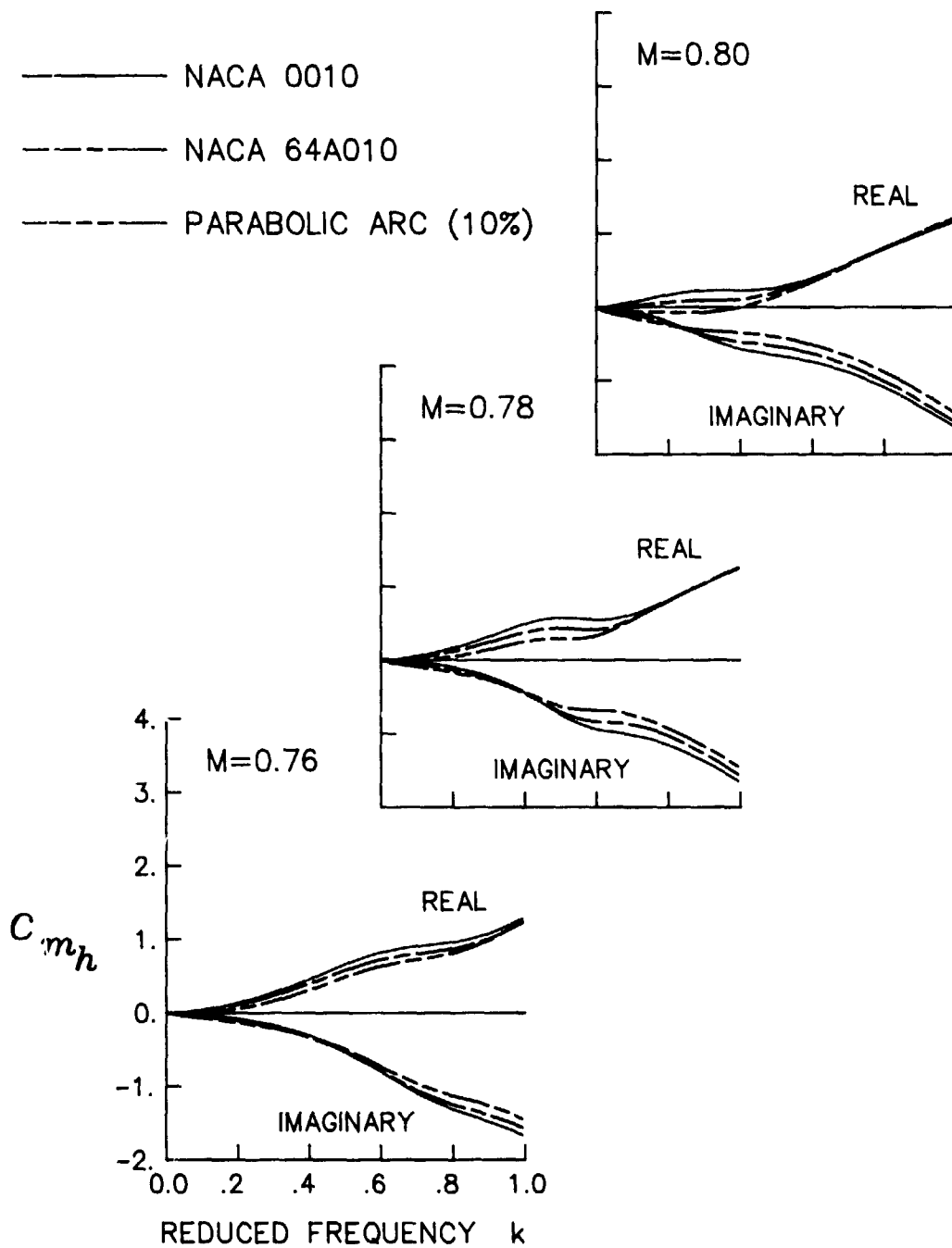
(a) Steady pressure distributions.

Figure 4. Results for airfoil shapes with no camber and $\alpha_o = 0^\circ$.



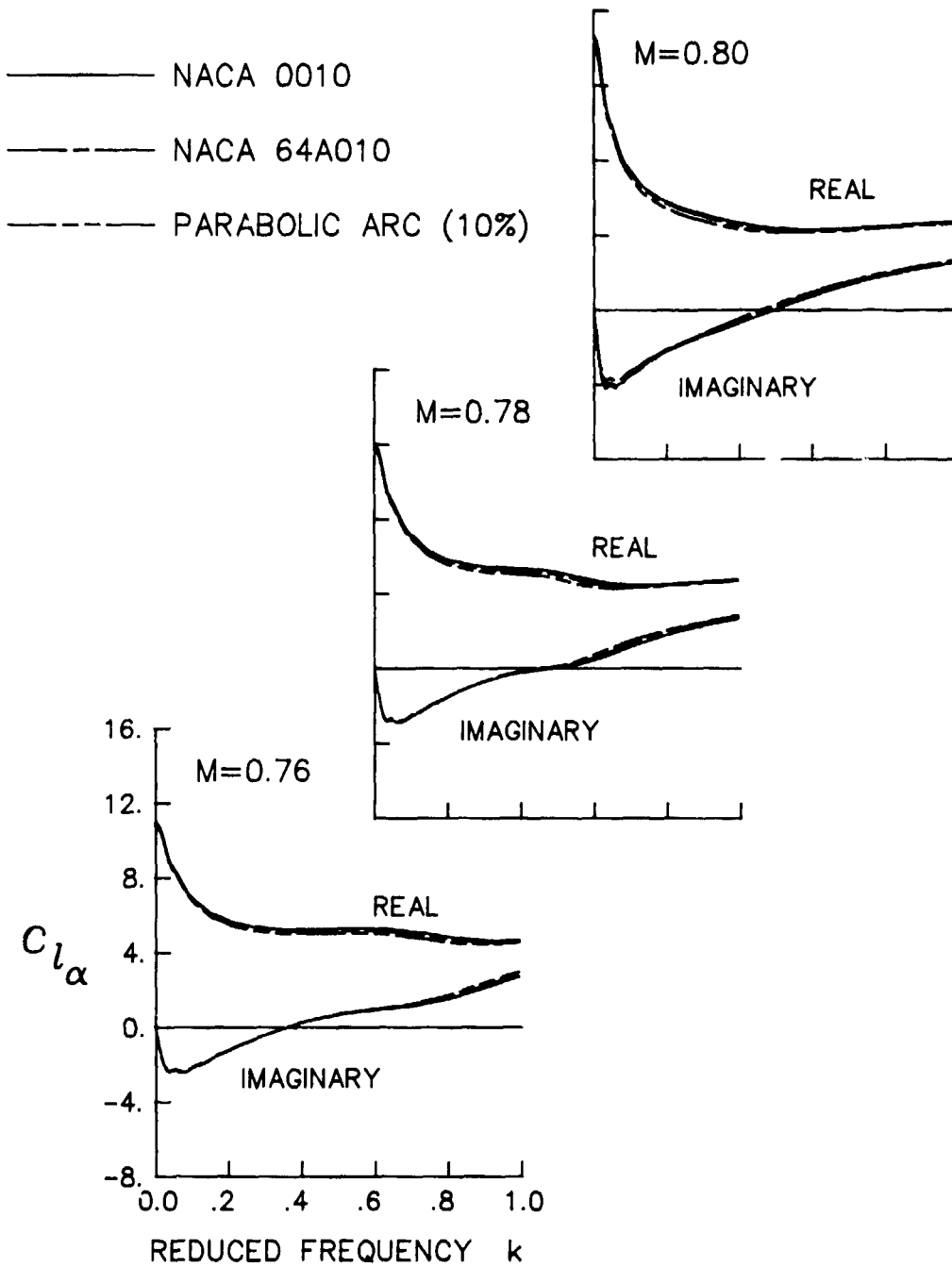
(b) Lift coefficient due to plunge.

Figure 4. Continued.



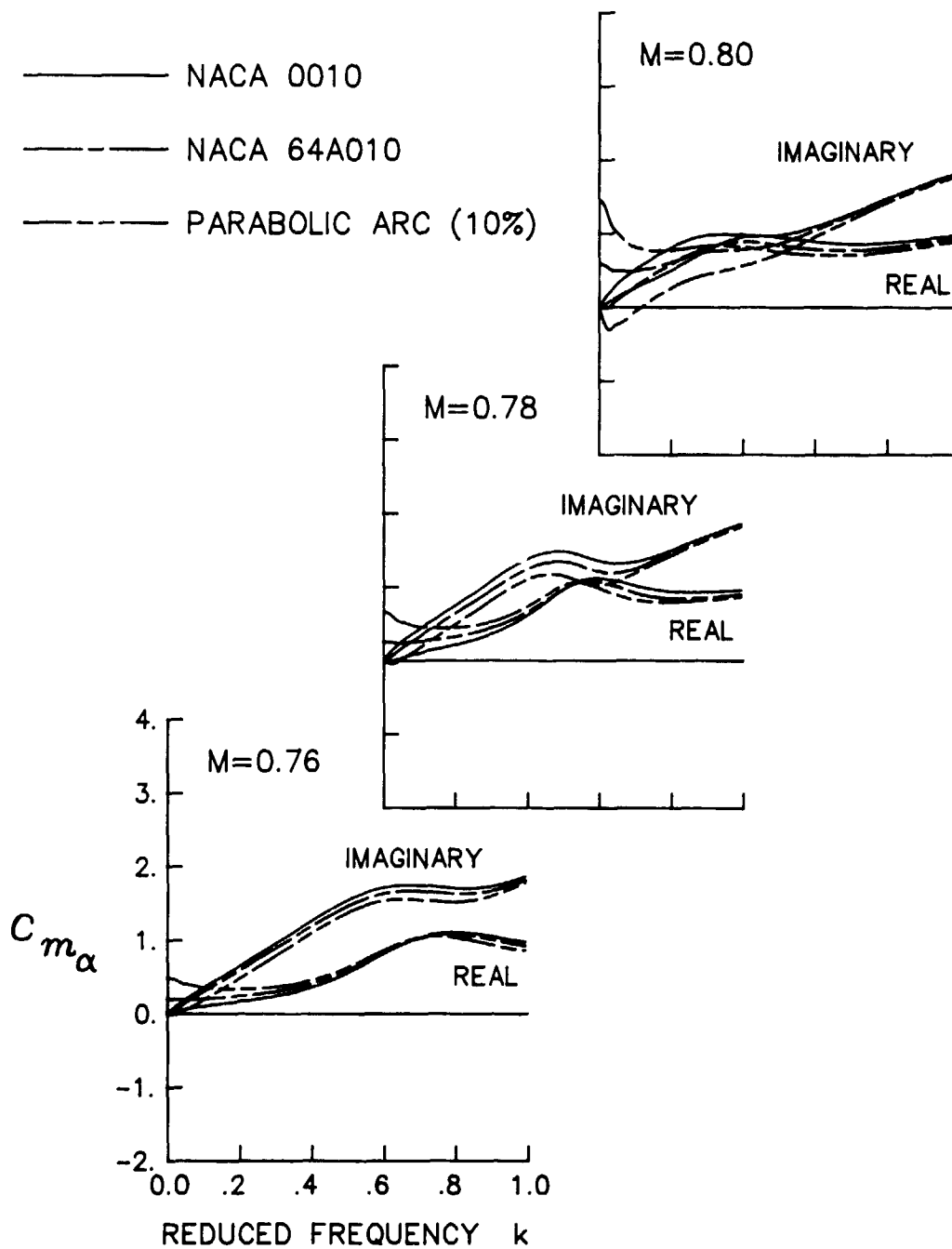
(c) Pitching-moment coefficient due to plunge.

Figure 4. Continued.



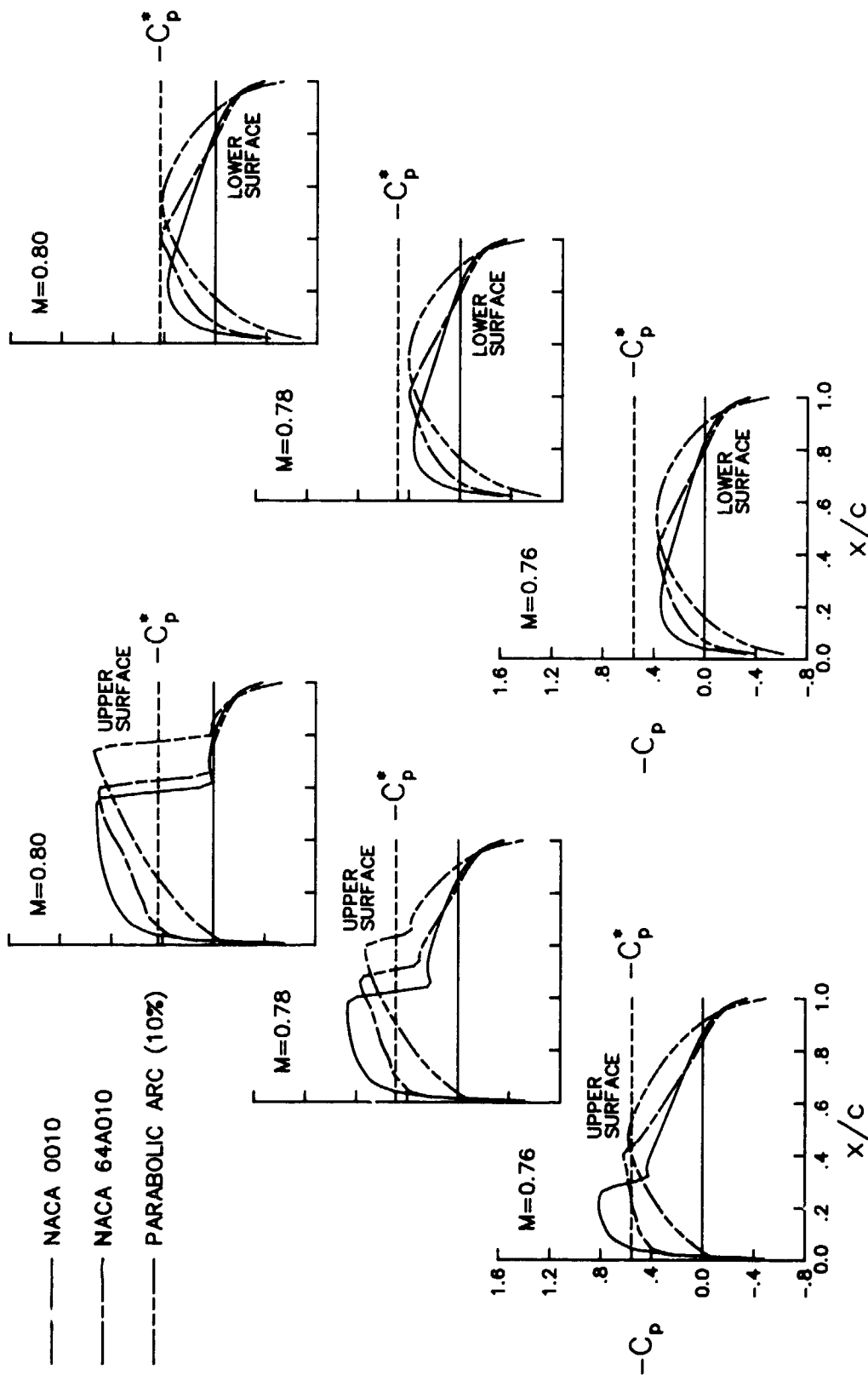
(d) Lift coefficient due to pitch.

Figure 4. Continued.



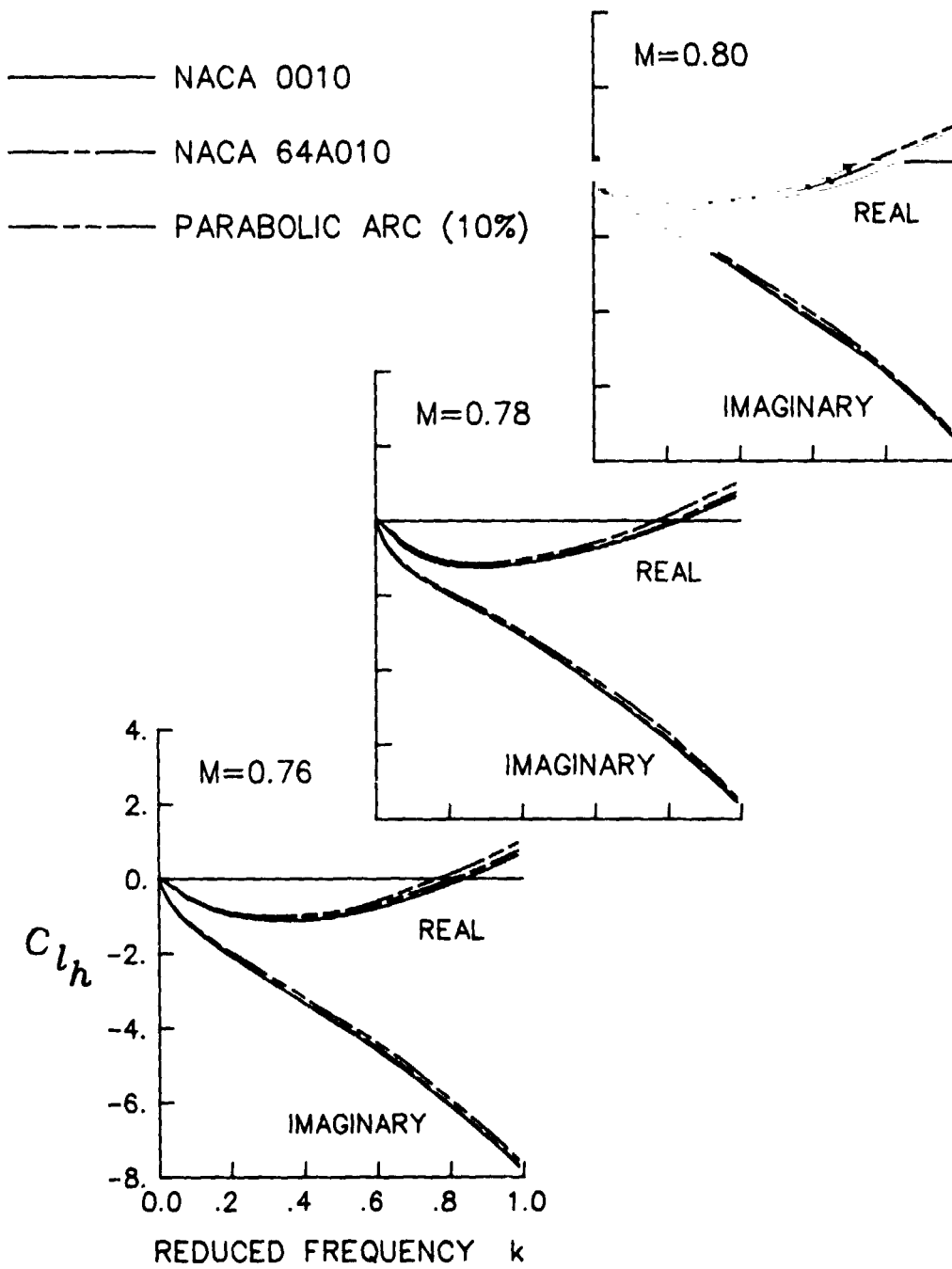
(e) Pitching-moment coefficient due to pitch.

Figure 4. Concluded.



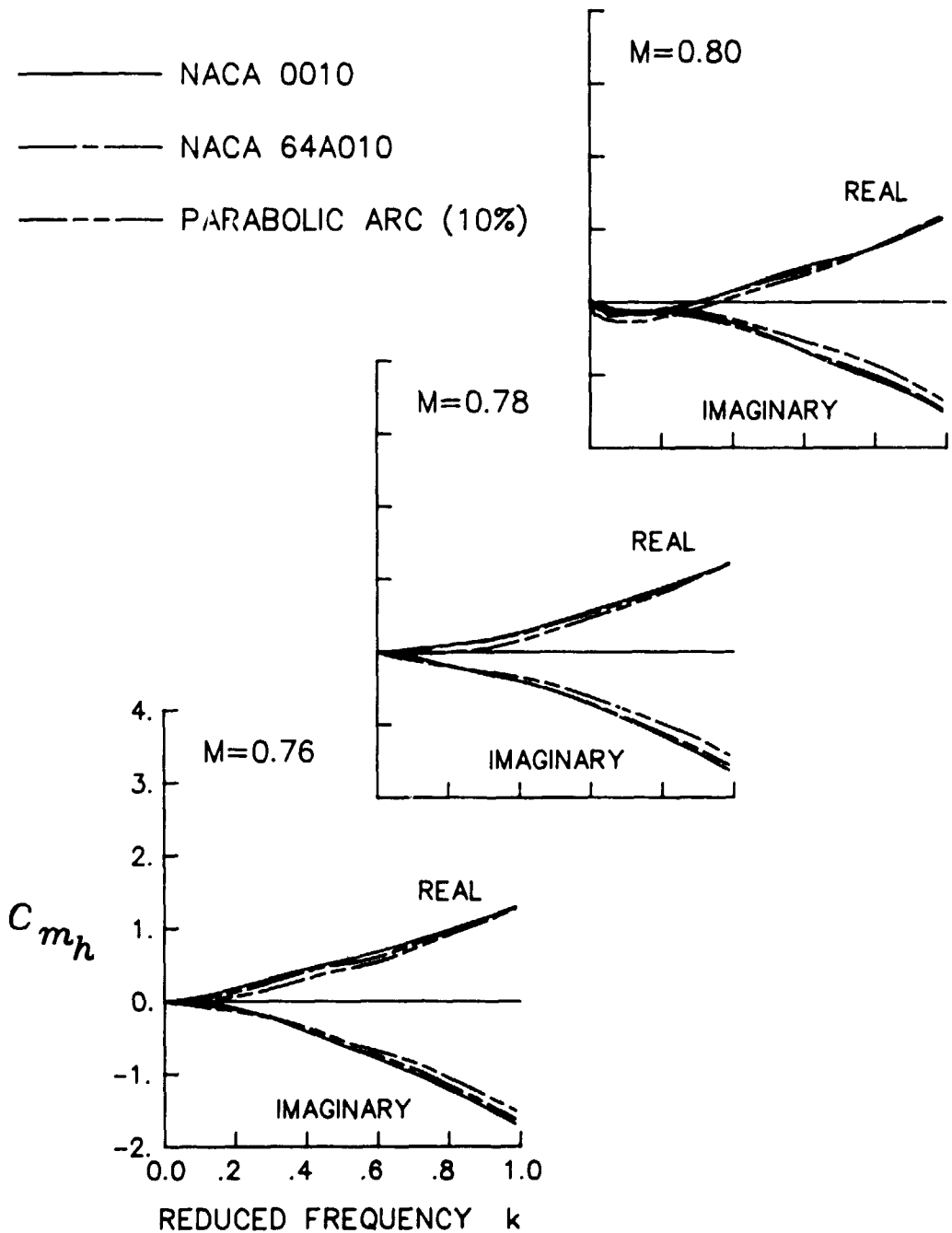
(a) Steady pressure distributions for airfoil upper and lower surfaces.

Figure 5. Results for airfoil shapes with no camber and $\alpha_0 = 1.0^\circ$.



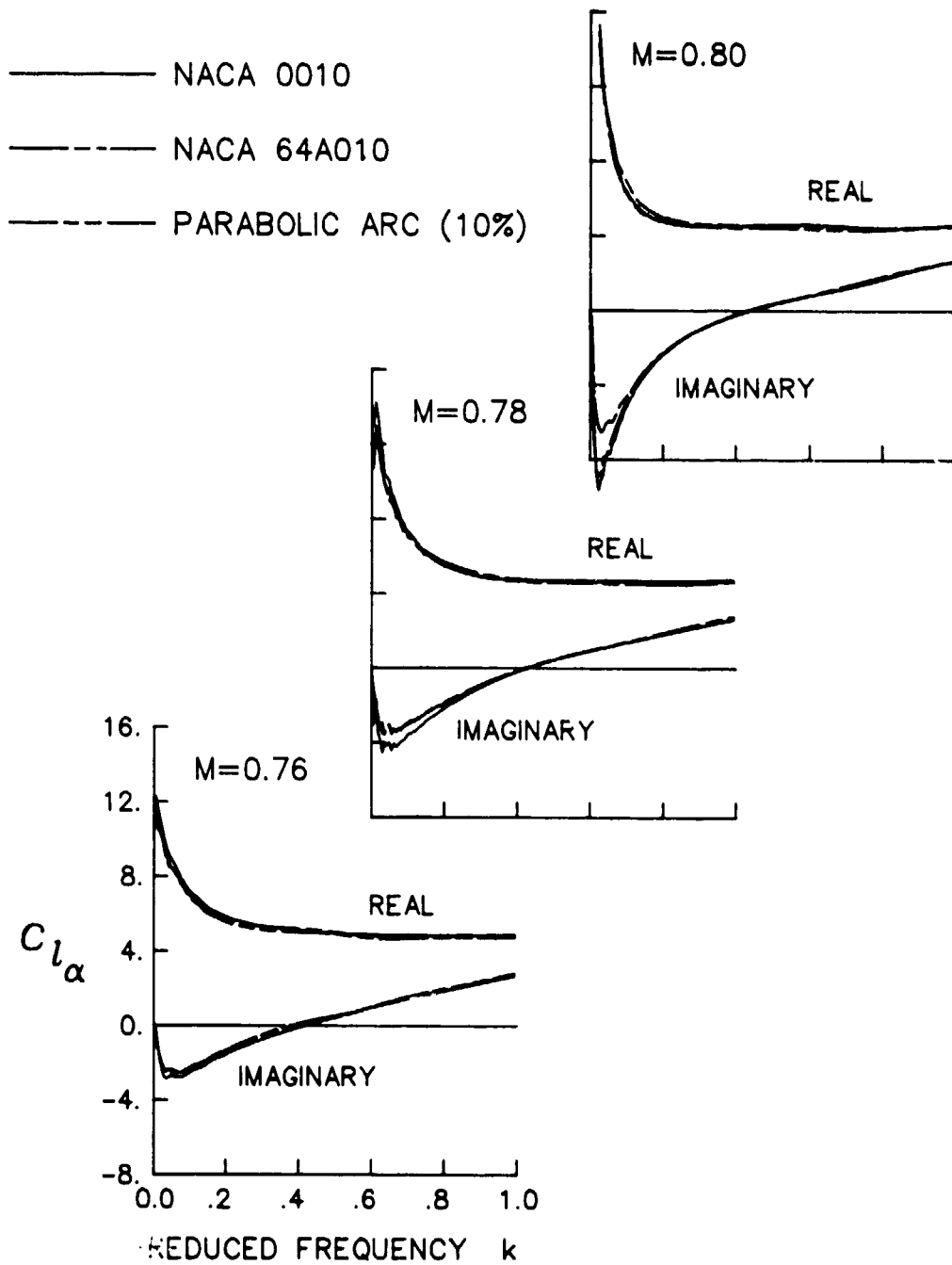
(b) Lift coefficient due to plunge.

Figure 5. Continued.



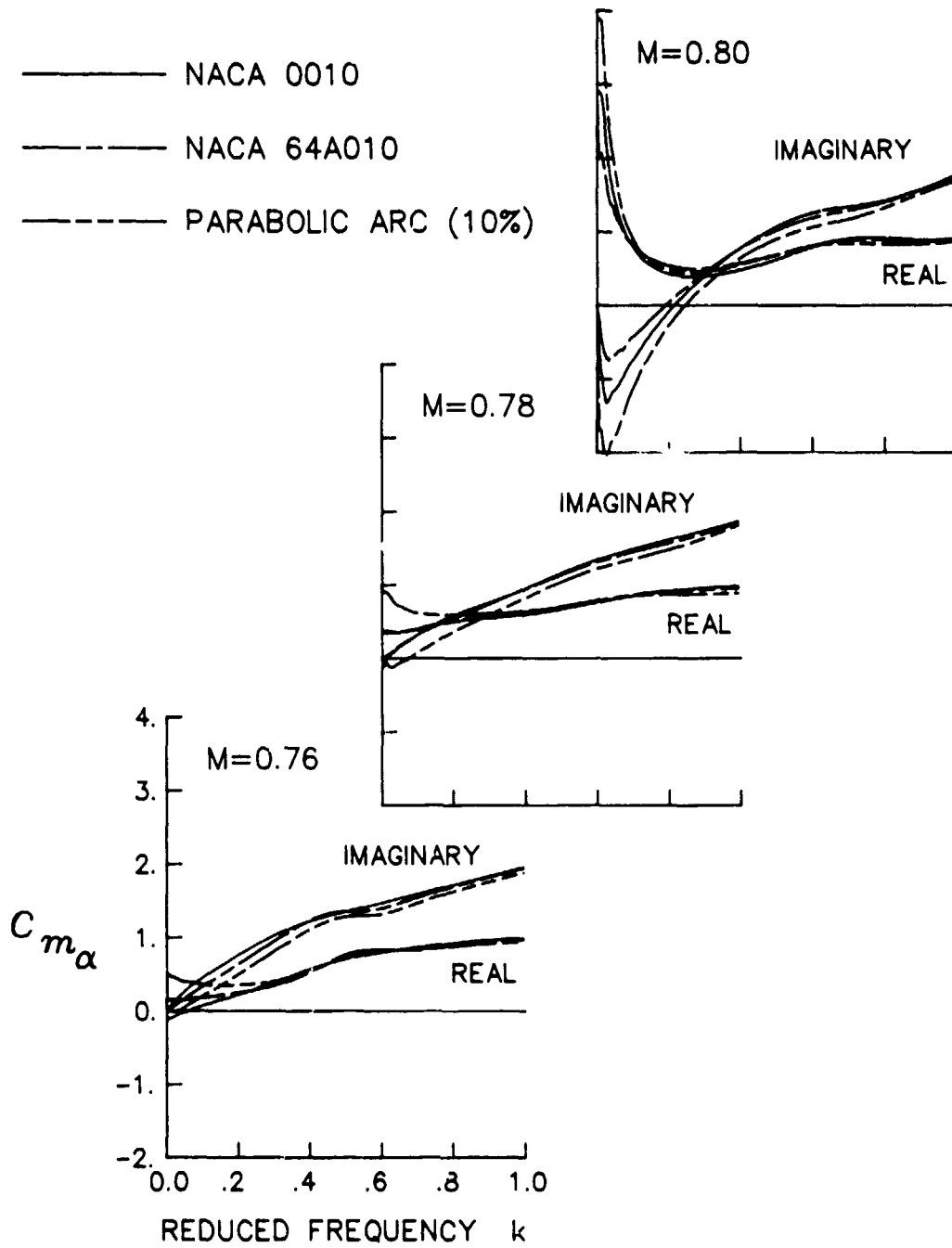
(c) Pitching-moment coefficient due to plunge.

Figure 5. Continued.



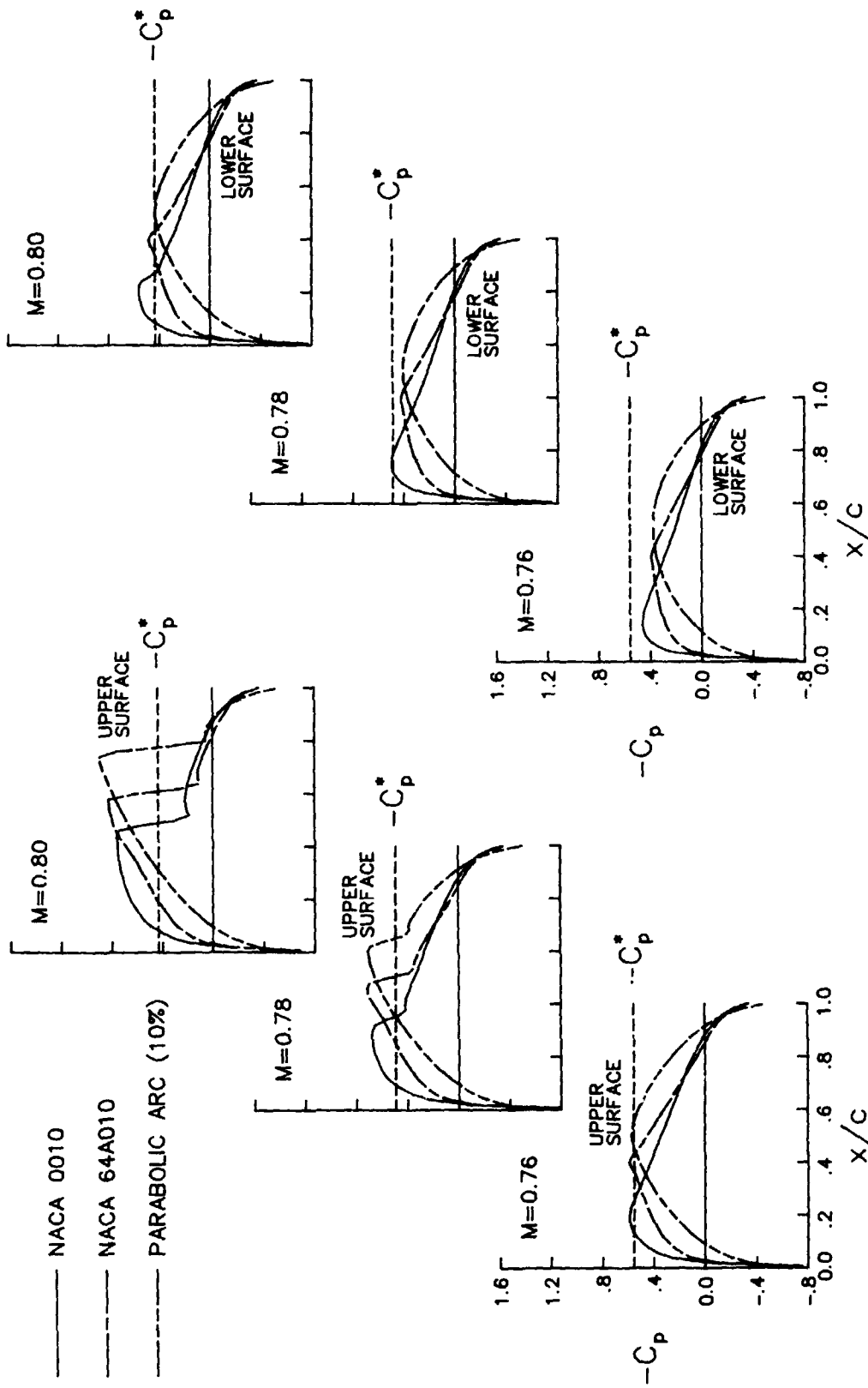
(d) Lift coefficient due to pitch.

Figure 5. Continued.



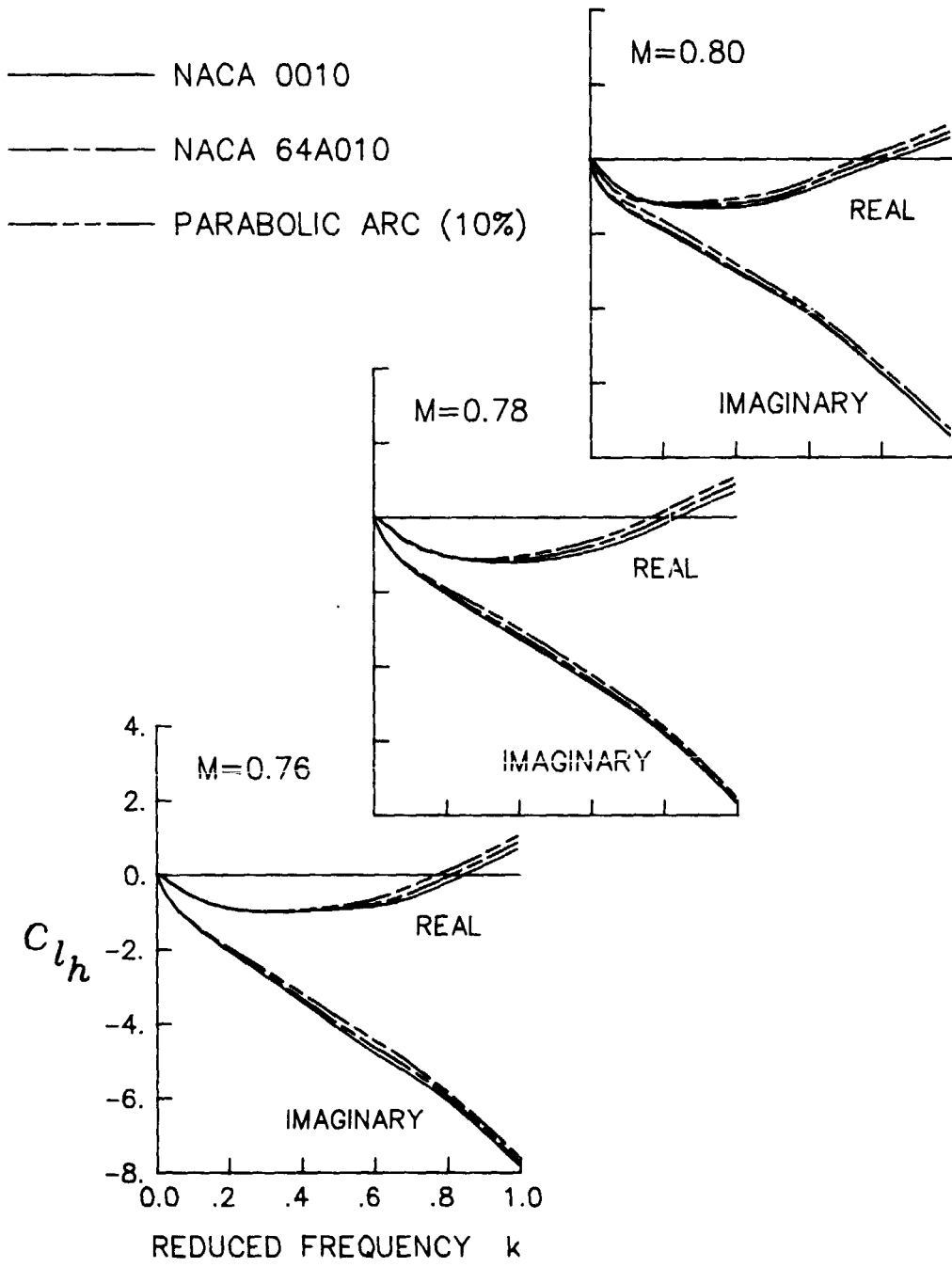
(e) Pitching-moment coefficient due to pitch.

Figure 5. Concluded.



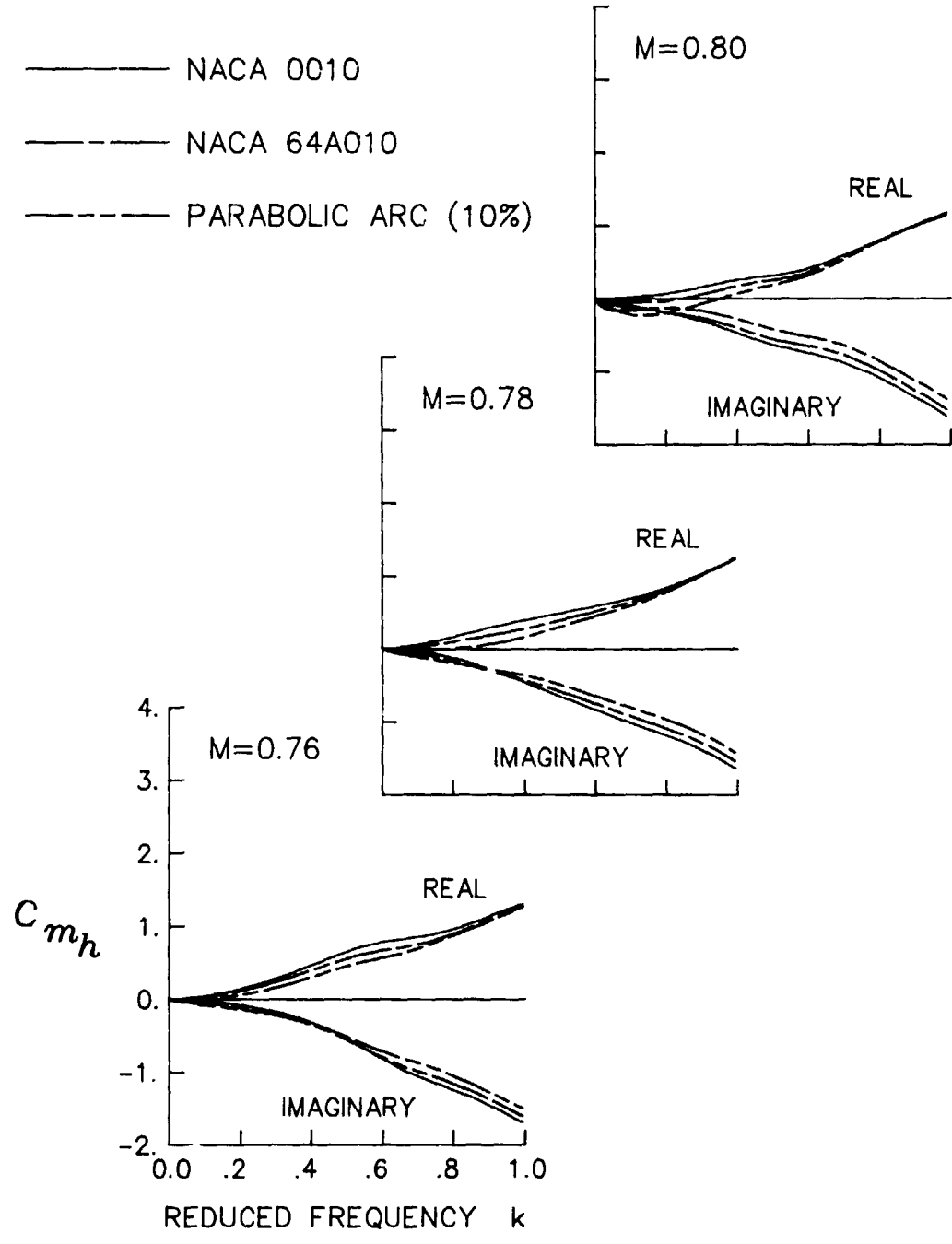
(a) Steady pressure distributions for airfoil upper and lower surface.

Figure 6. Results for airfoil shapes with $d = 0.00436$ and $\alpha_o = 0^\circ$.



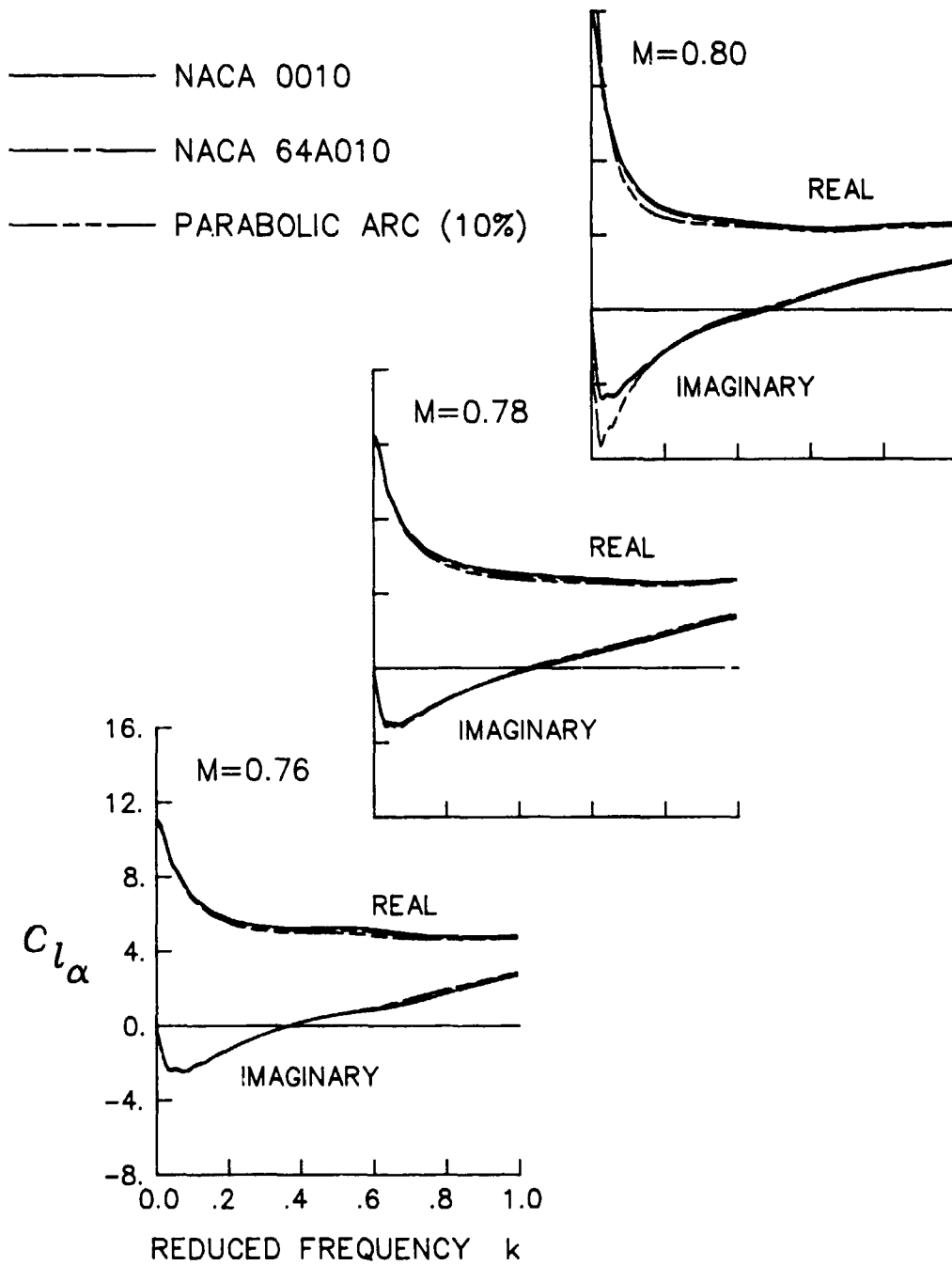
(b) Lift coefficient due to plunge.

Figure 6. Continued.



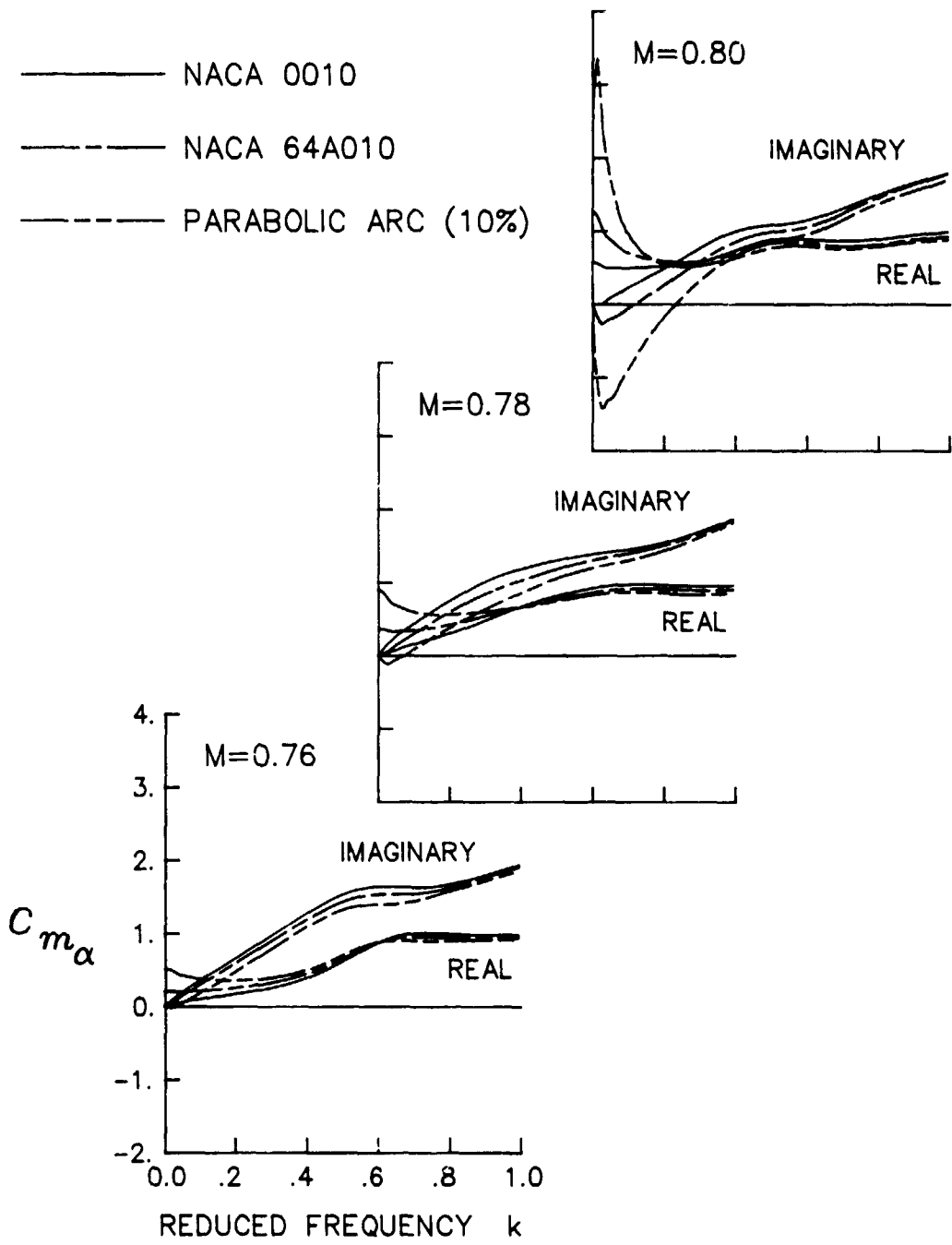
(c) Pitching-moment coefficient due to plunge.

Figure 6. Continued.



(d) Lift coefficient due to pitch.

Figure 6. Continued.



(e) Pitching-moment coefficient due to pitch.

Figure 6. Concluded.

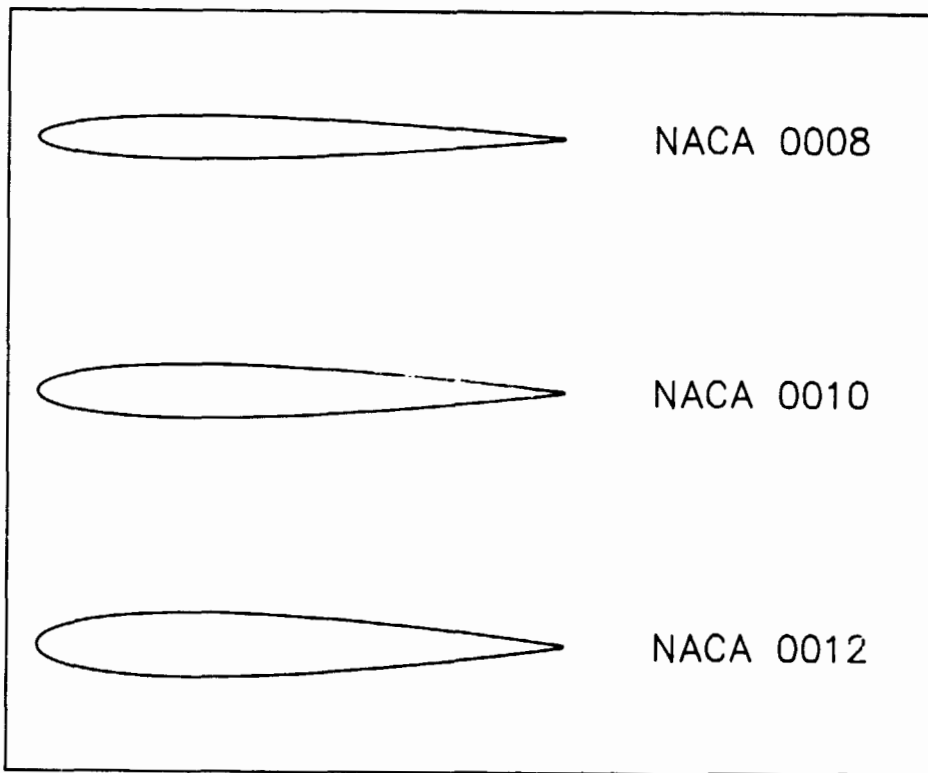


Figure 7. Profiles of NACA 0008, NACA 0010, and NACA 0012 airfoils used in thickness effects study.

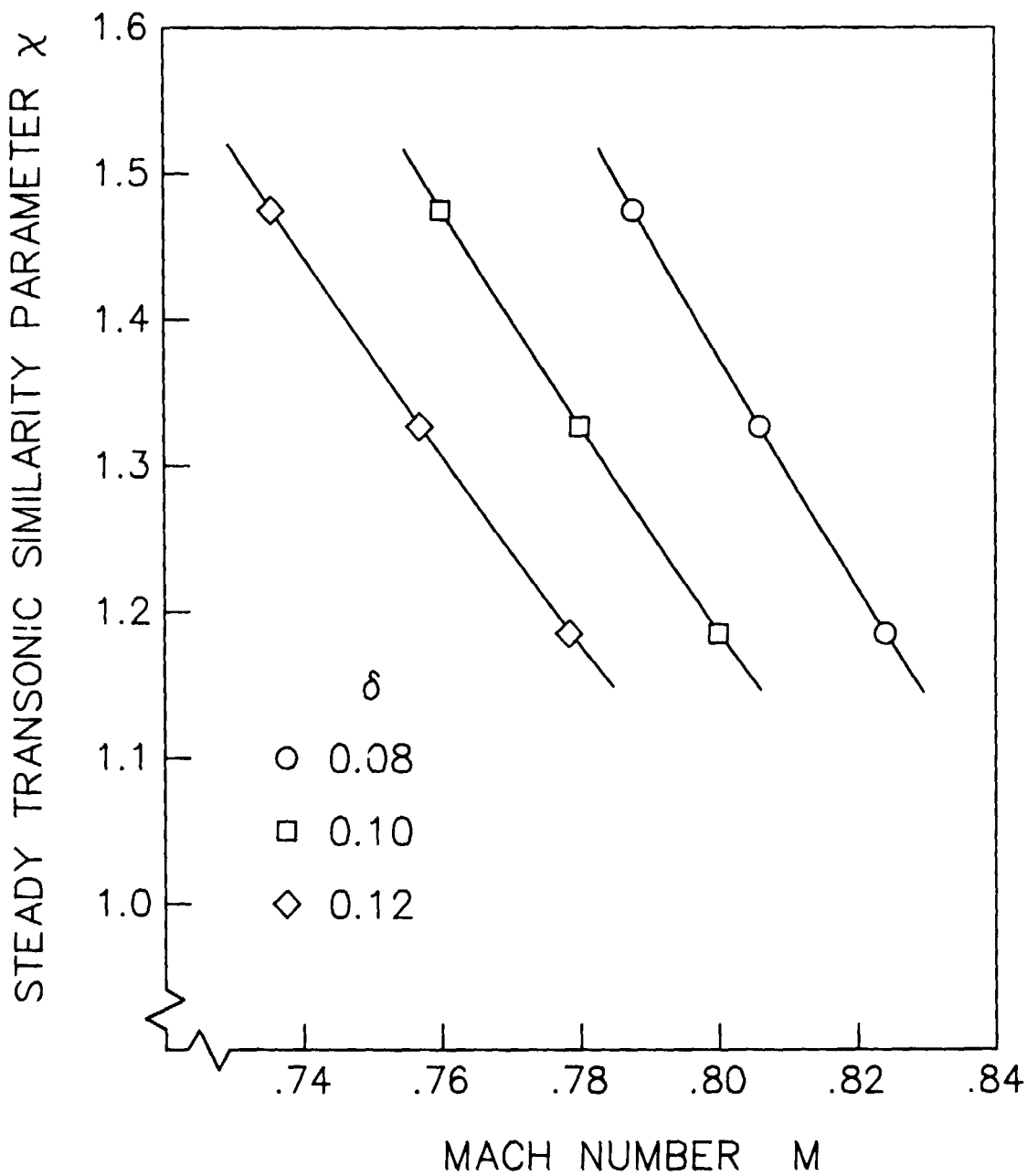
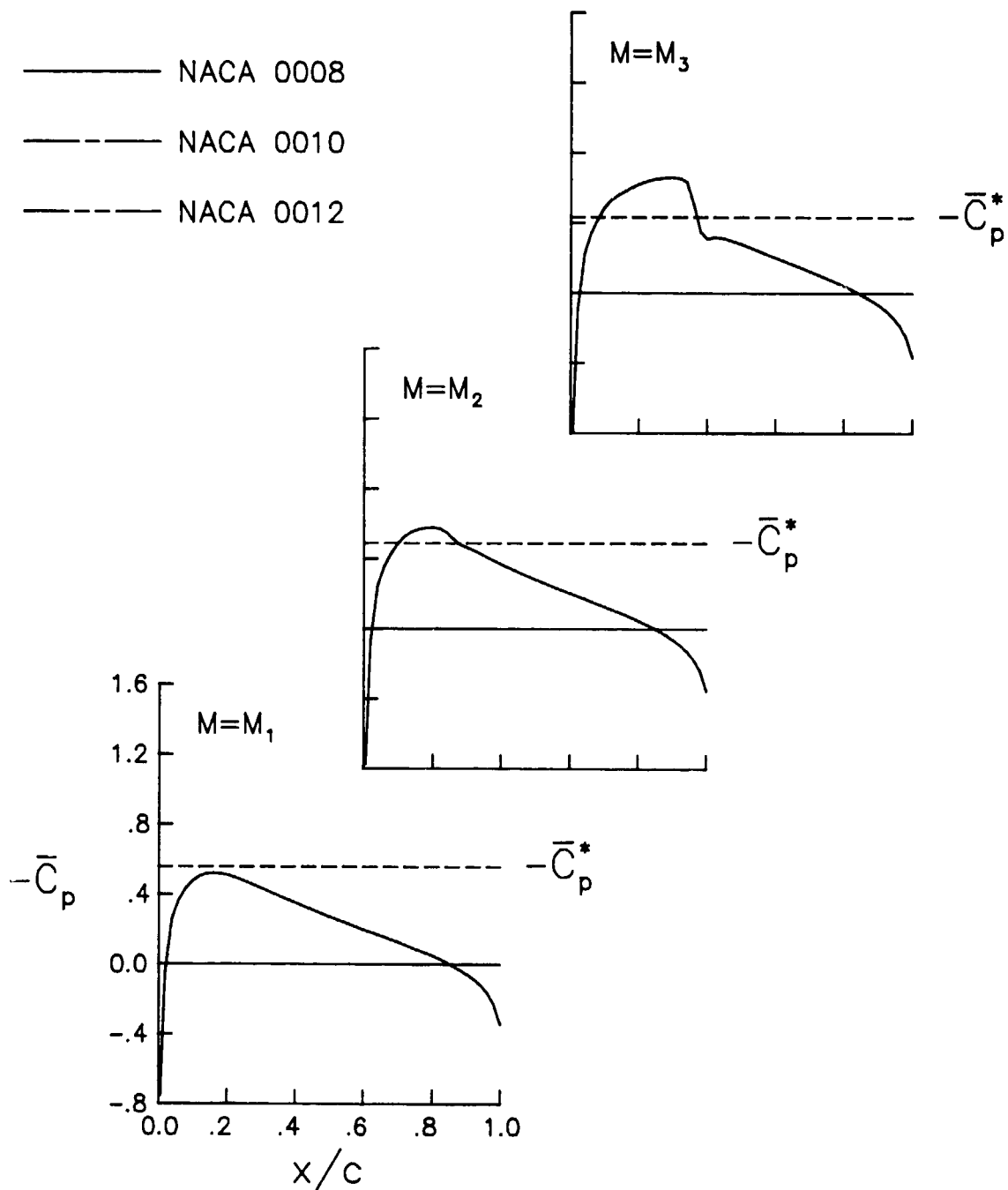
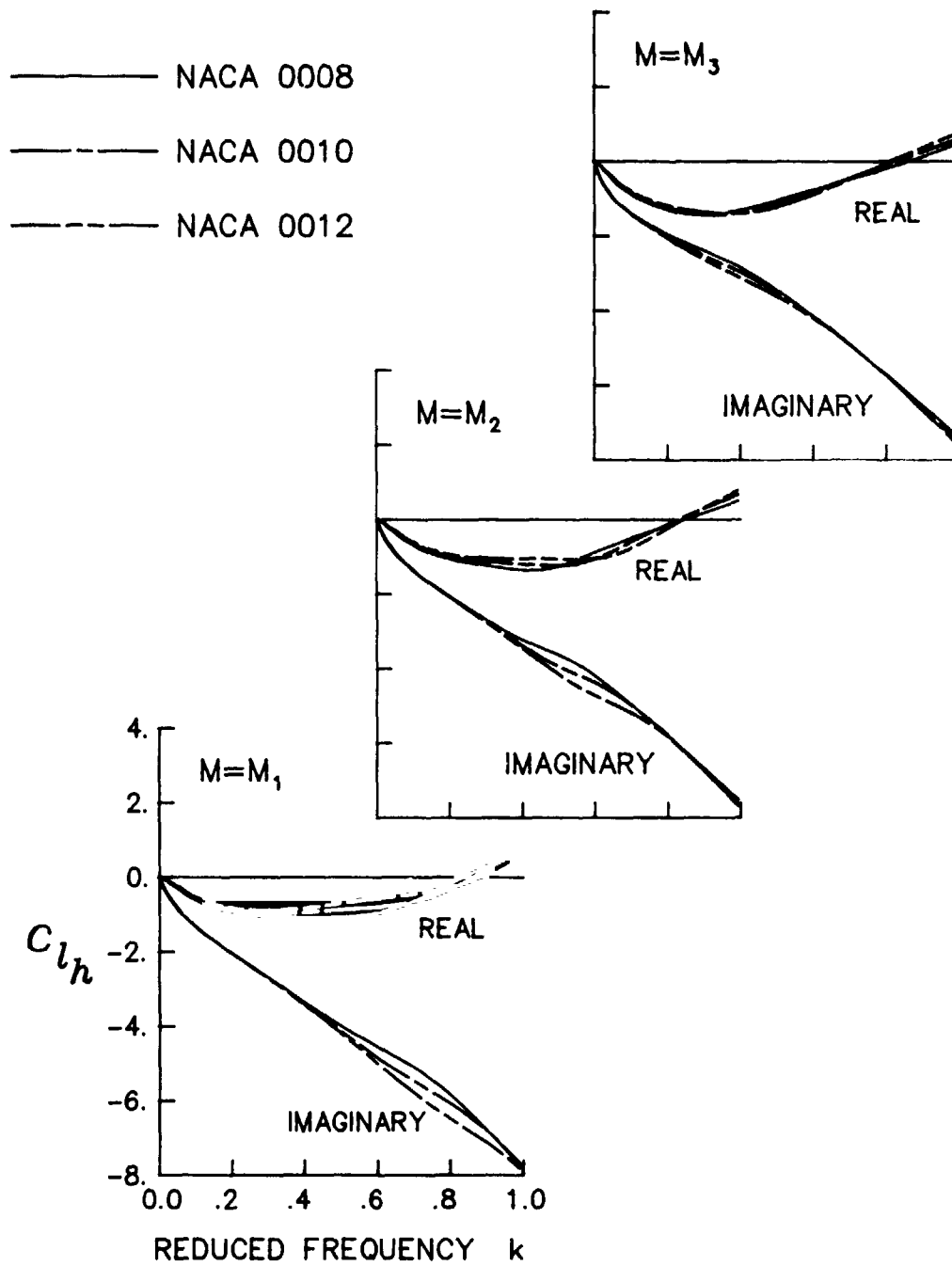


Figure 8. Variation of steady transonic similarity parameter with Mach number for $\delta = 0.08, 0.10,$ and 0.12 .



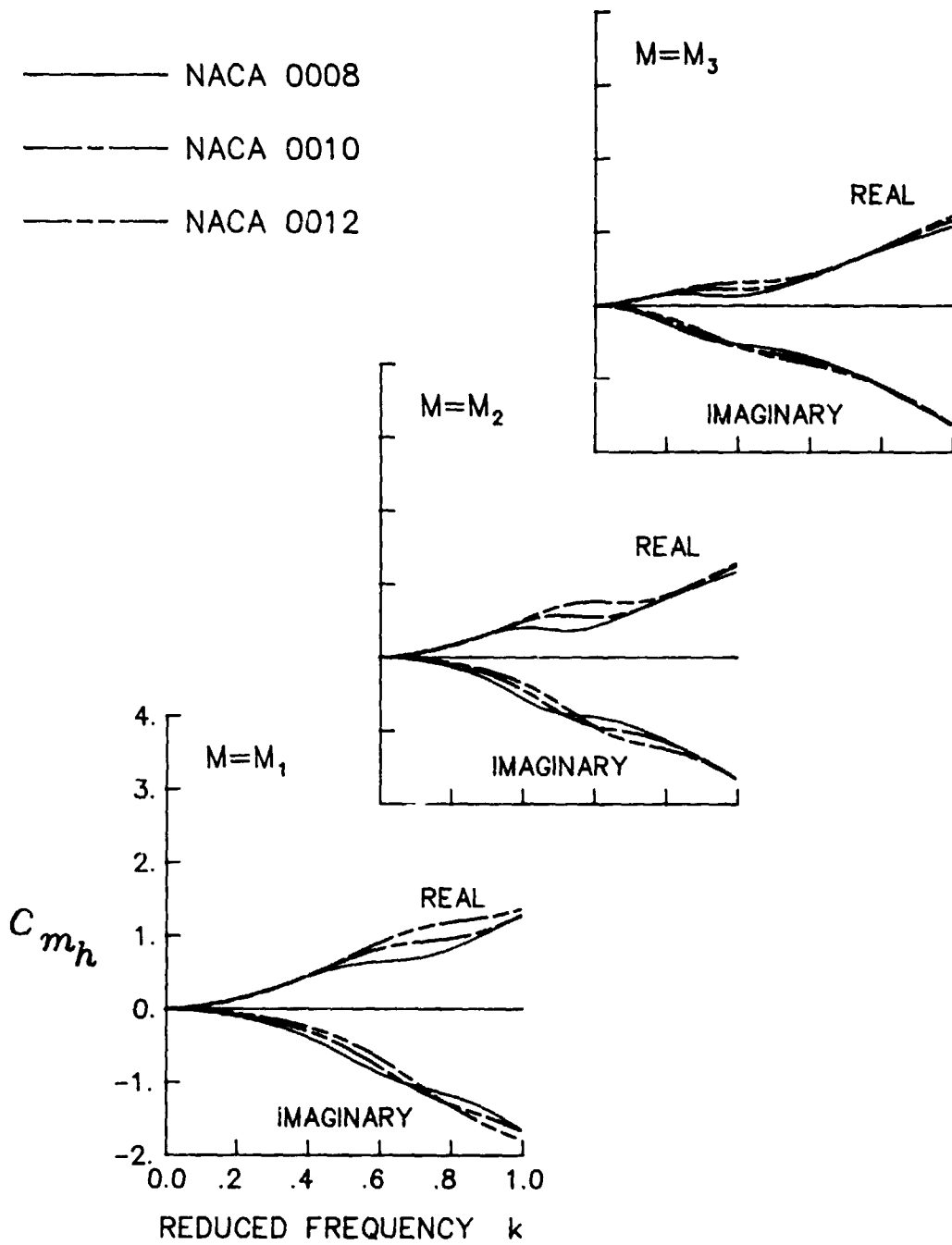
(a) Scaled steady pressure distributions.

Figure 9. Results for airfoil thicknesses with no camber and $\alpha_o = 0^\circ$.



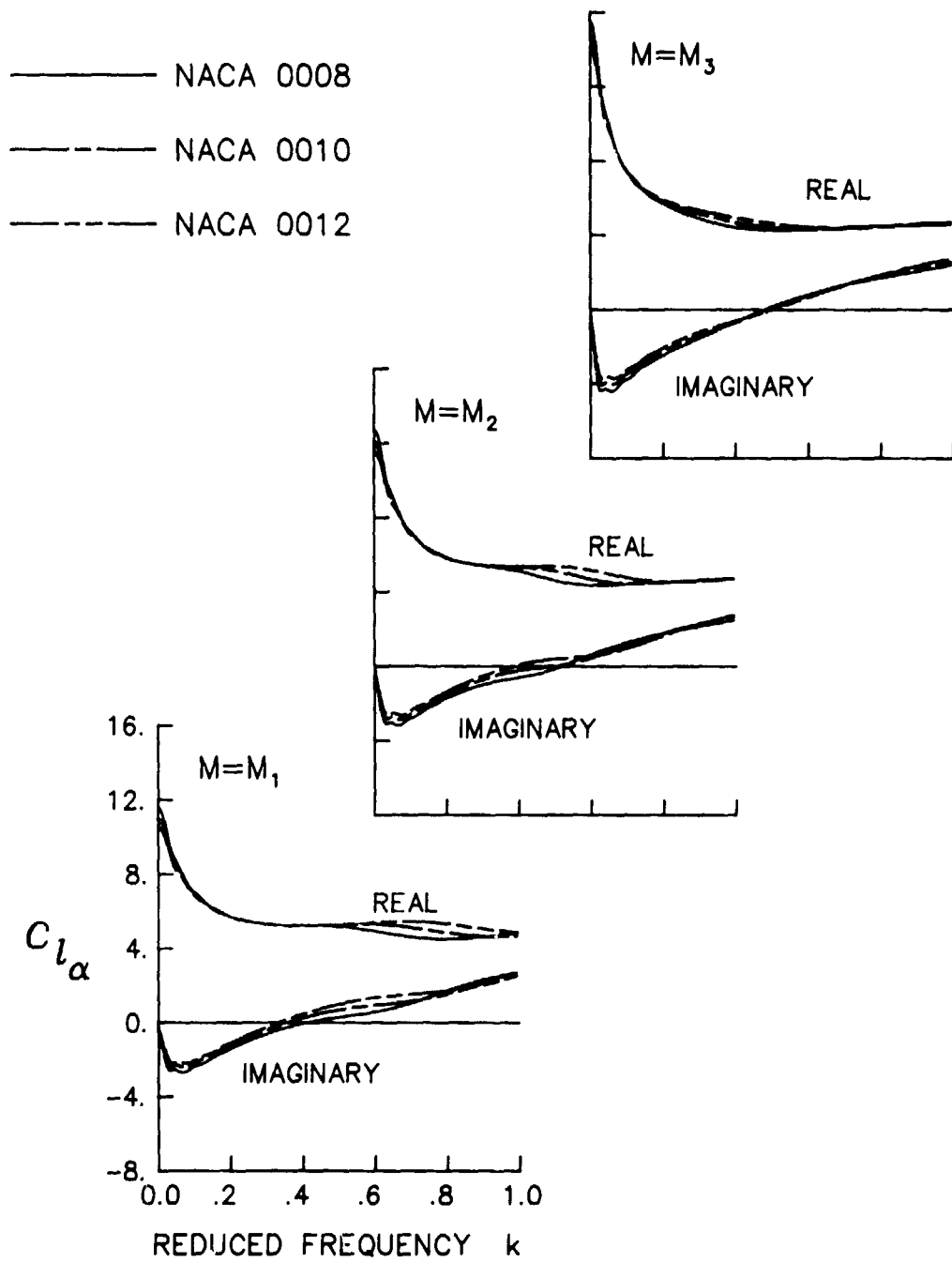
(b) Lift coefficient due to plunge.

Figure 9. Continued.



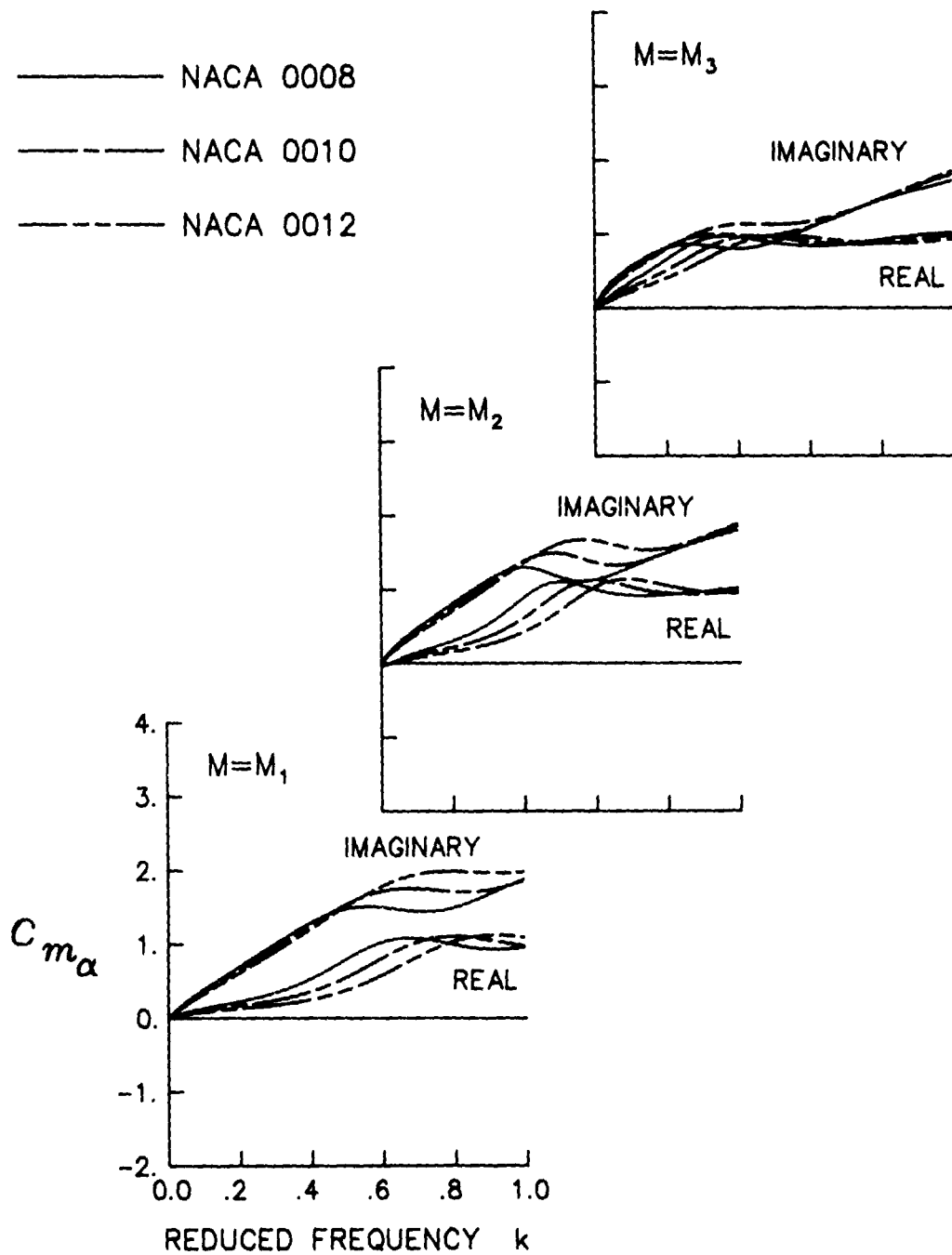
(c) Pitching-moment coefficient due to plunge.

Figure 9. Continued.



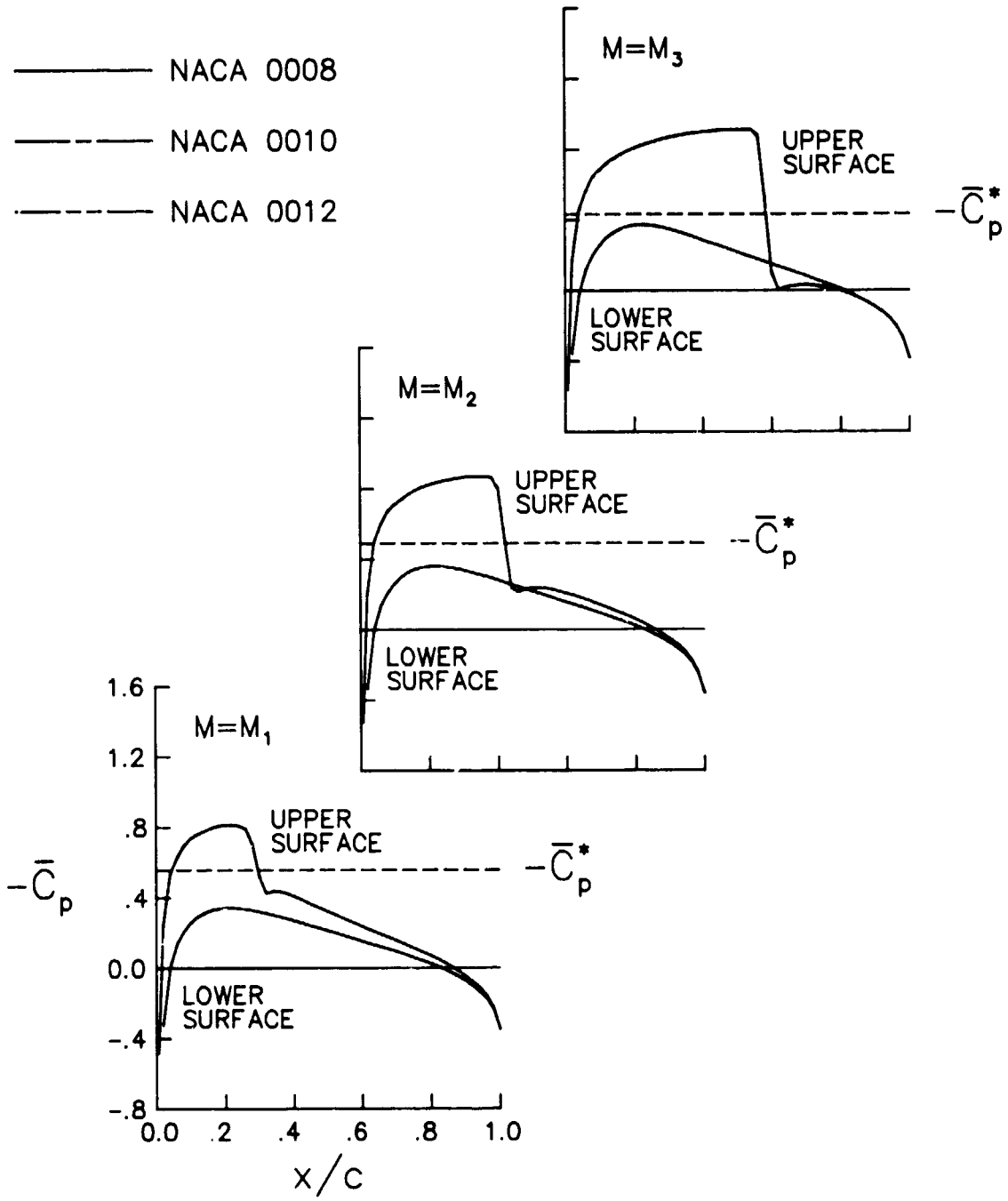
(d) Lift coefficient due to pitch.

Figure 9. Continued.



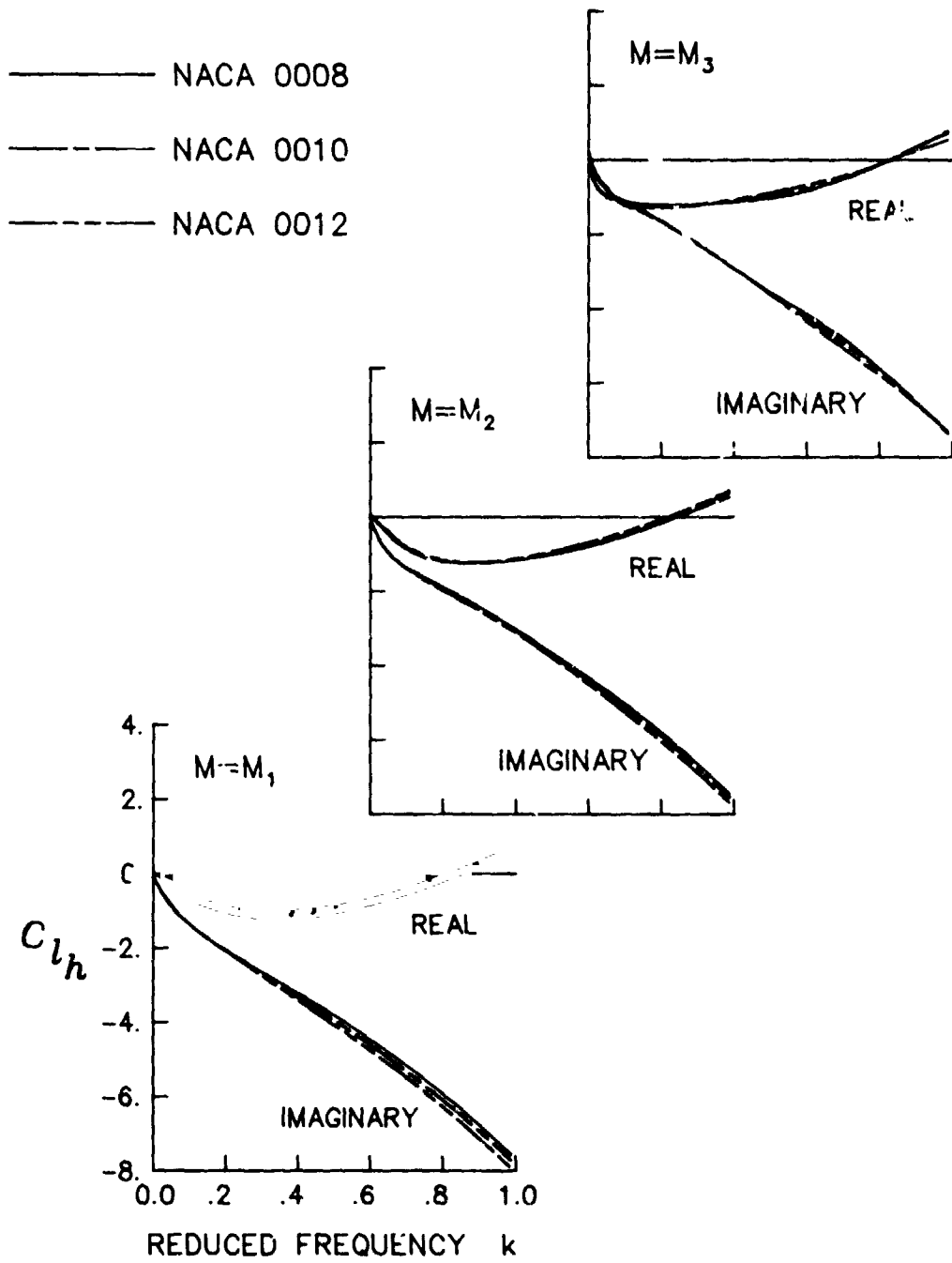
(e) Pitching-moment coefficient due to pitch.

Figure 9. Concluded.



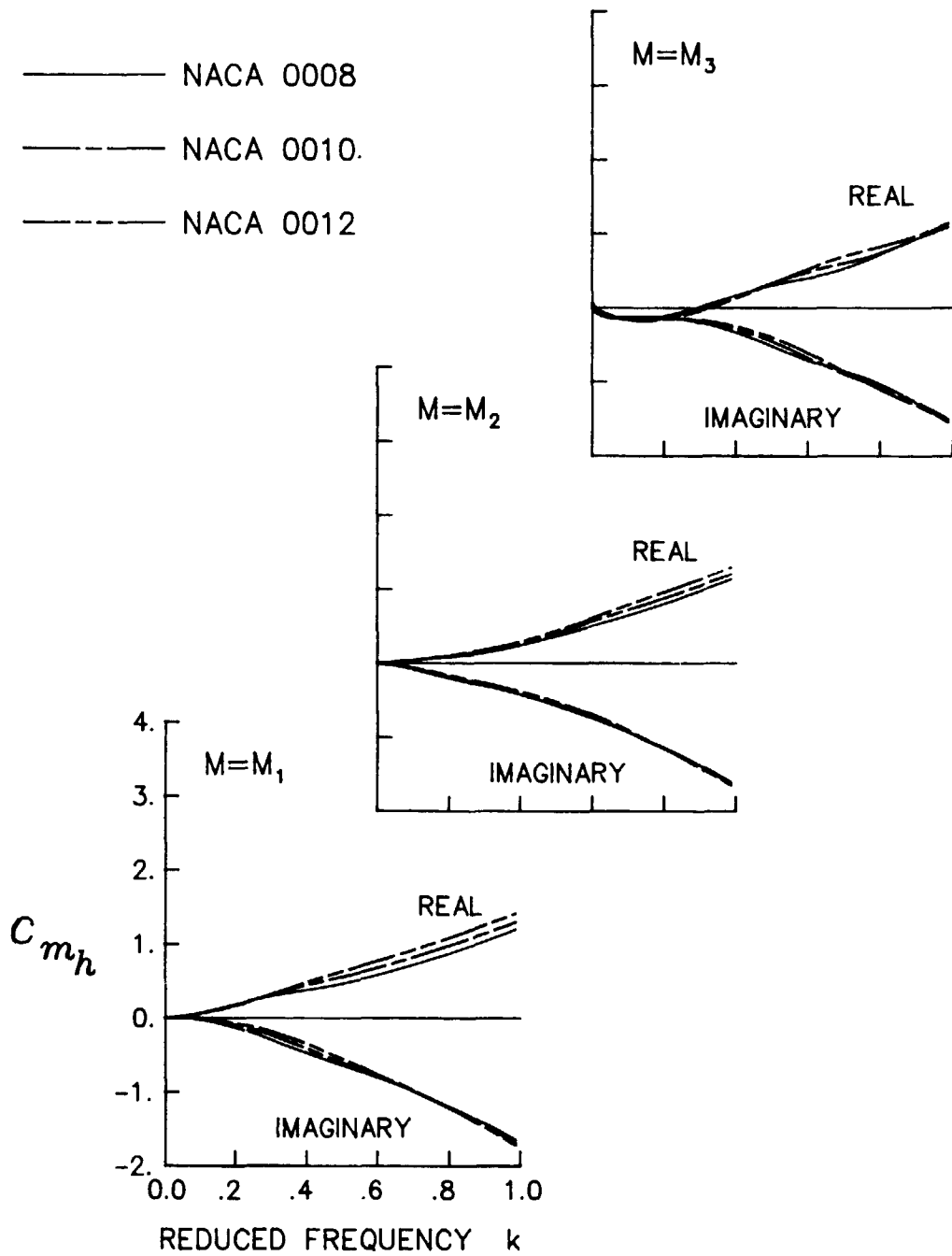
(a) Scaled steady pressure distributions.

Figure 10. Results for airfoil thicknesses with no camber and $\alpha_o = 1.0^\circ$.



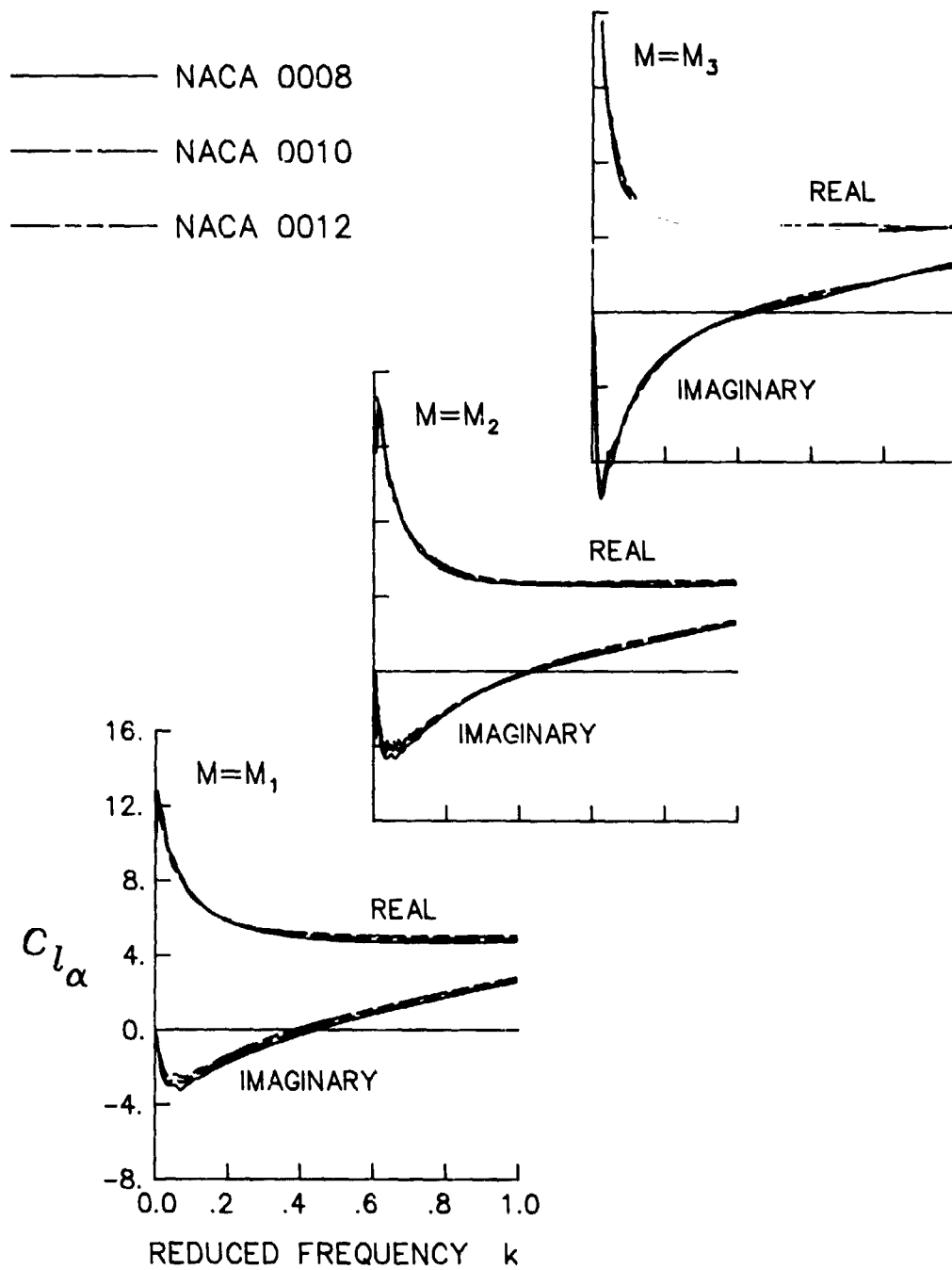
(b) Lift coefficient due to plunge.

Figure 10. Continued.



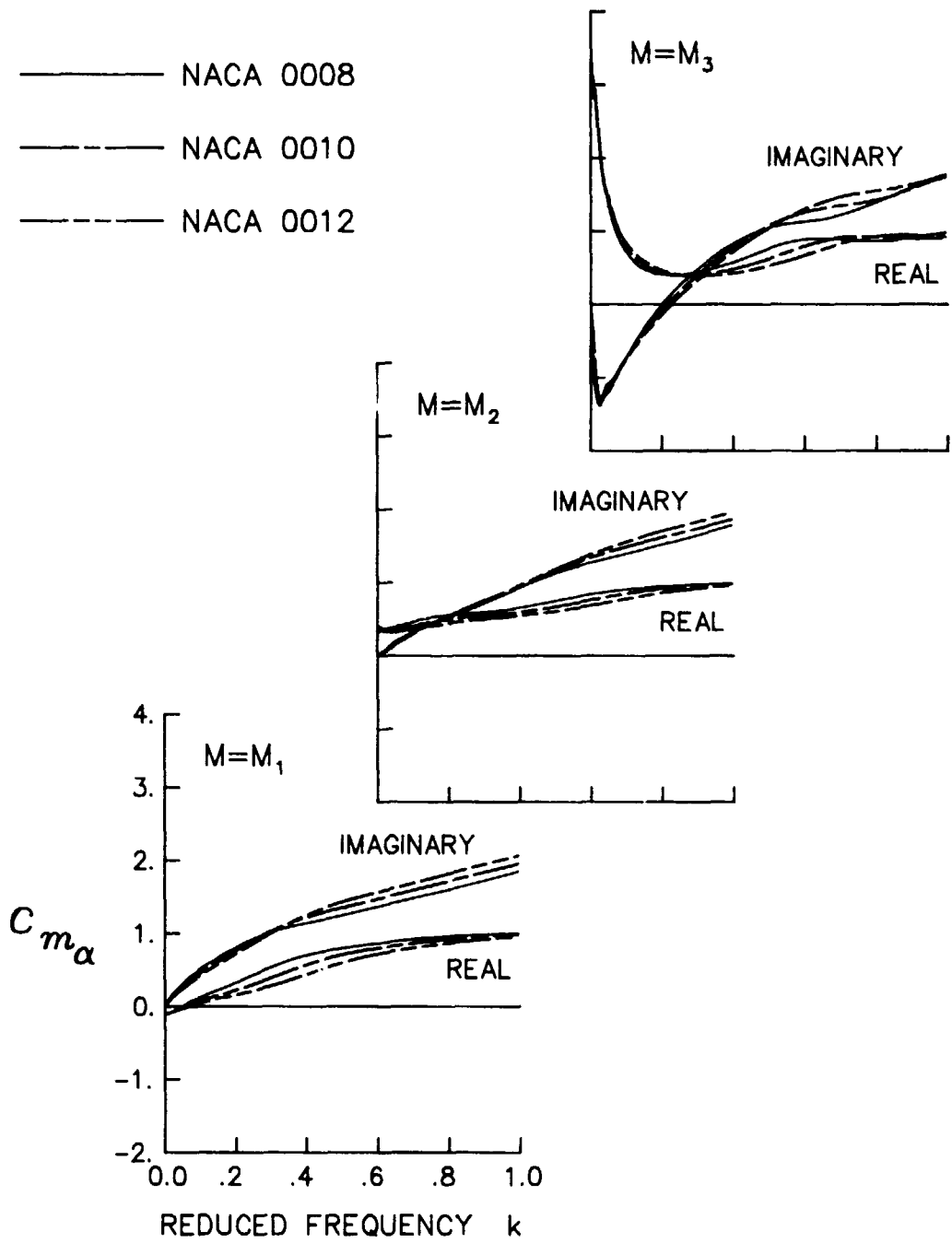
(c) Pitching-moment coefficient due to plunge.

Figure 10. Continued.



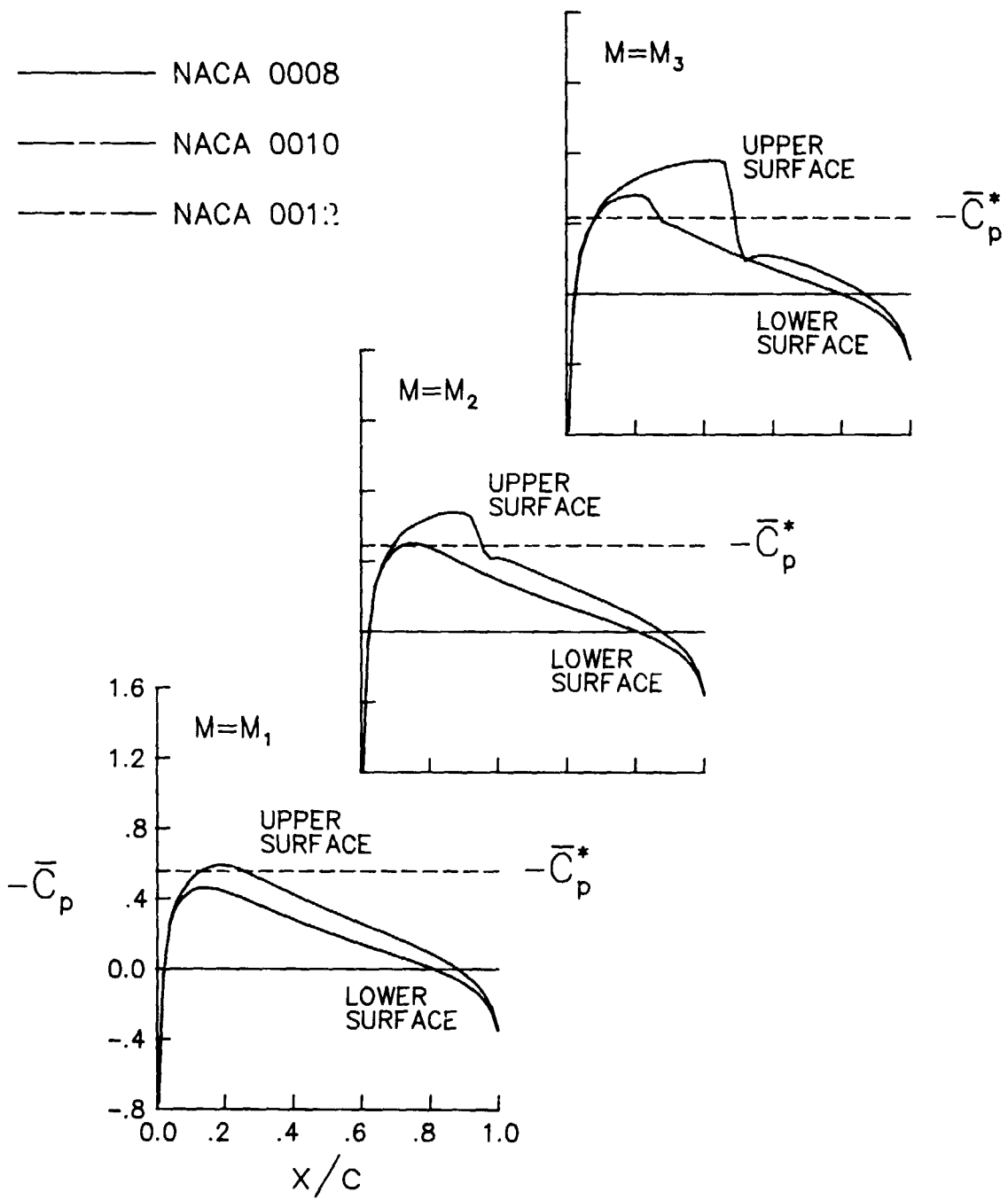
(d) Lift coefficient due to pitch.

Figure 10. Continued.



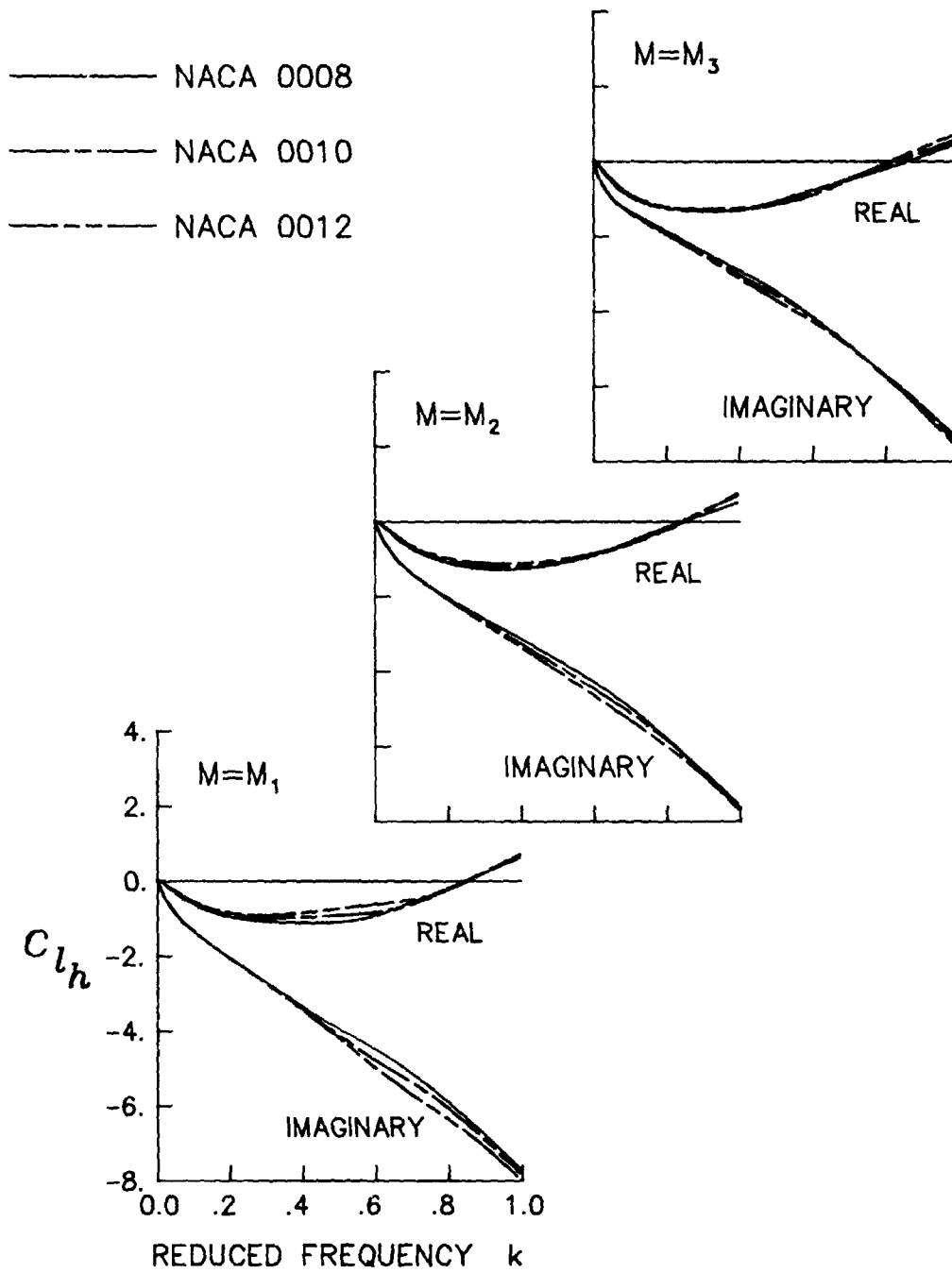
(e) Pitching-moment coefficient due to pitch.

Figure 10. Concluded.



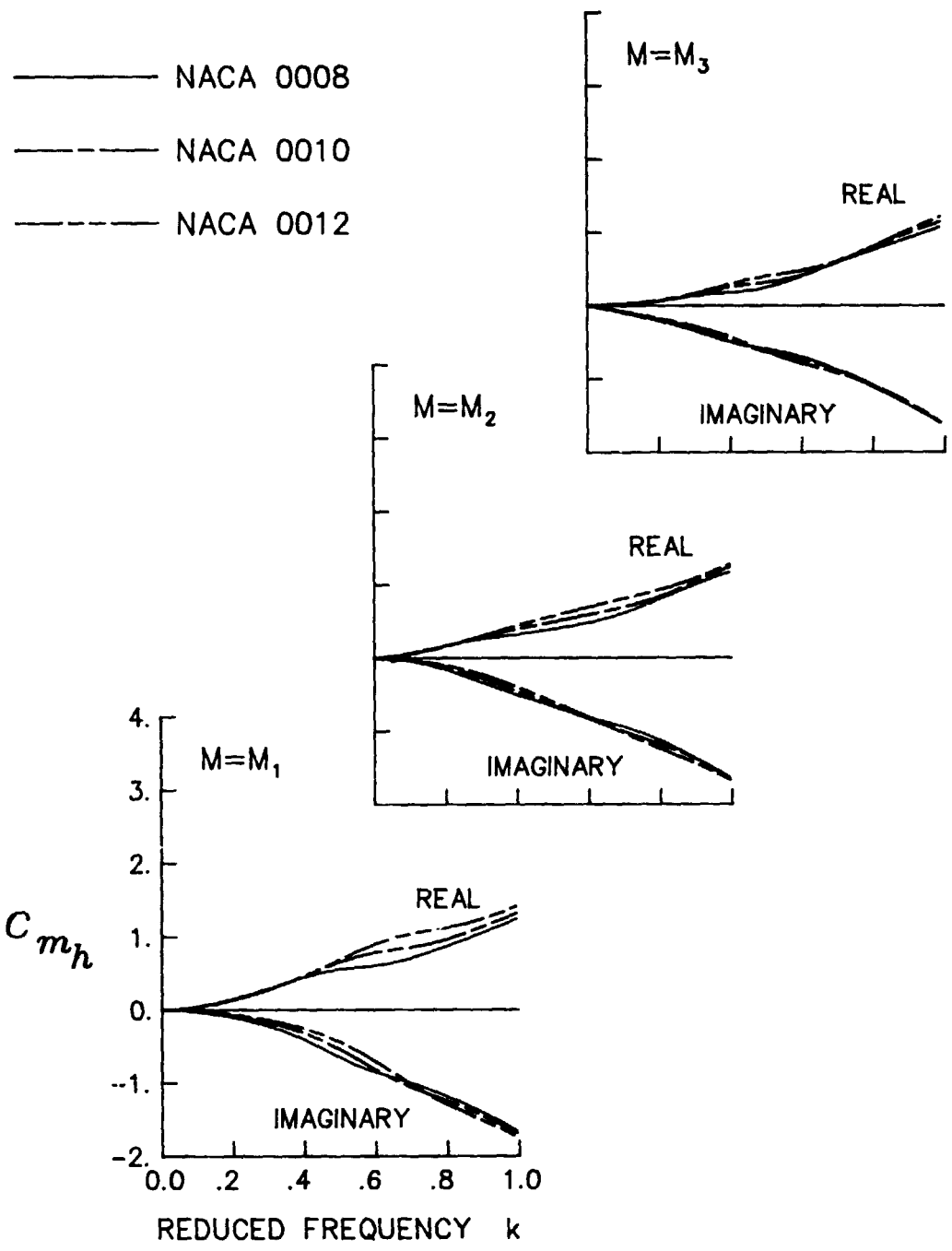
(a) Scaled steady pressure distributions.

Figure 11. Results for airfoil thicknesses with $\bar{d} = 0.00436$ and $\bar{\alpha}_0 = 0^\circ$.



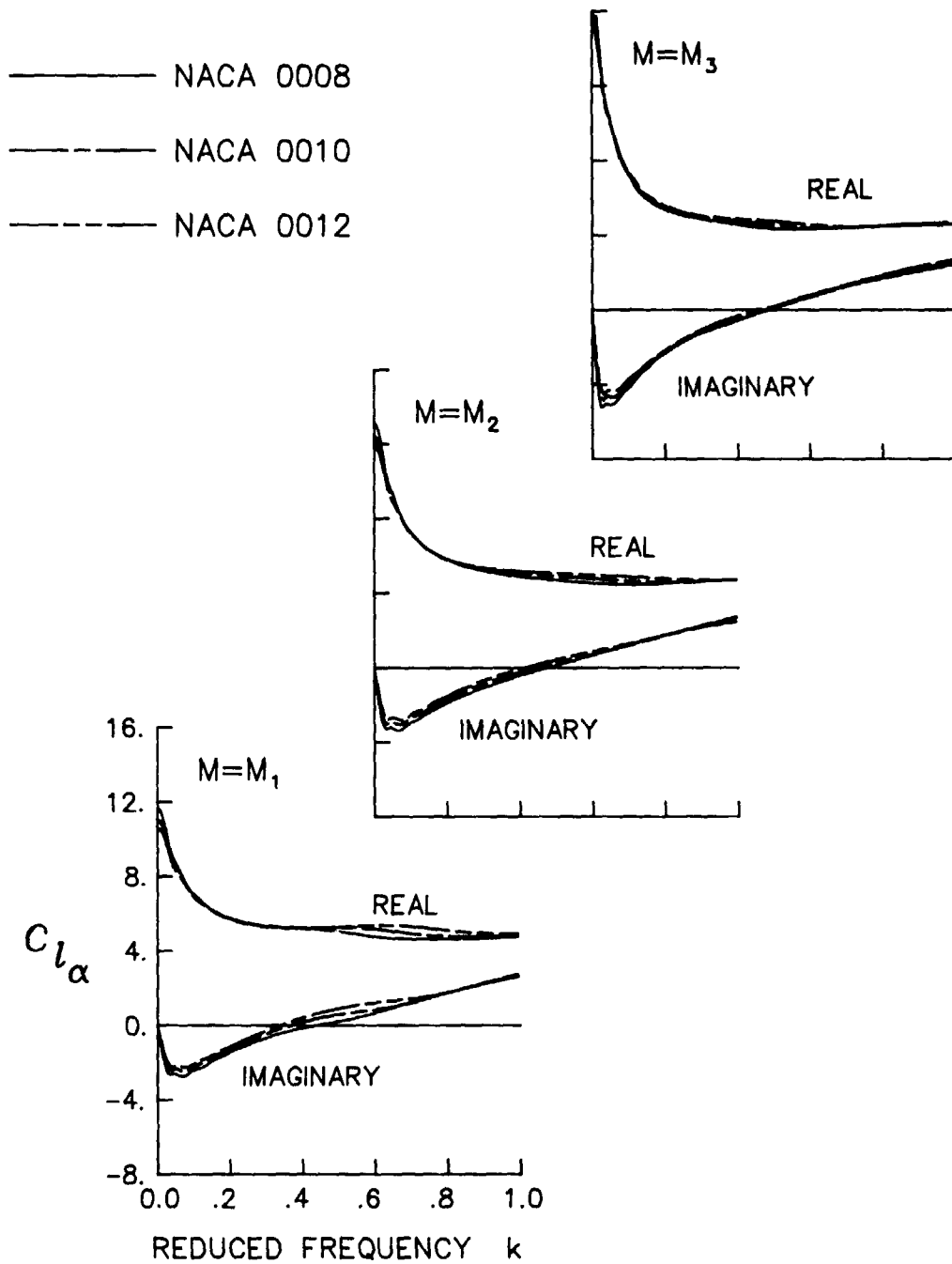
(b) Lift coefficient due to plunge.

Figure 11. Continued.



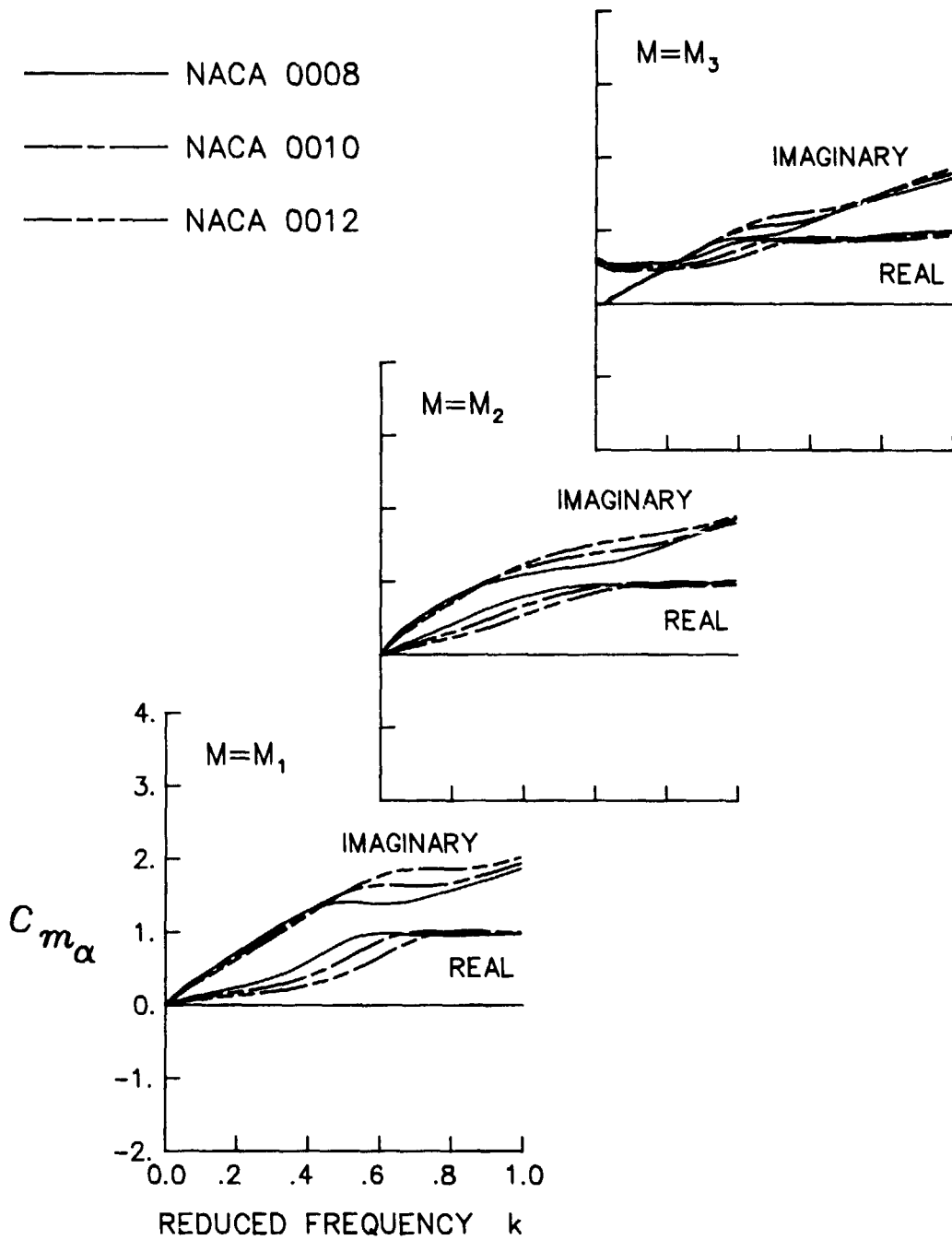
(c) Pitching-moment coefficient due to plunge.

Figure 11. Continued.



(d) Lift coefficient due to pitch.

Figure 11. Continued.



(e) Pitching-moment coefficient due to pitch.

Figure 11. Concluded.

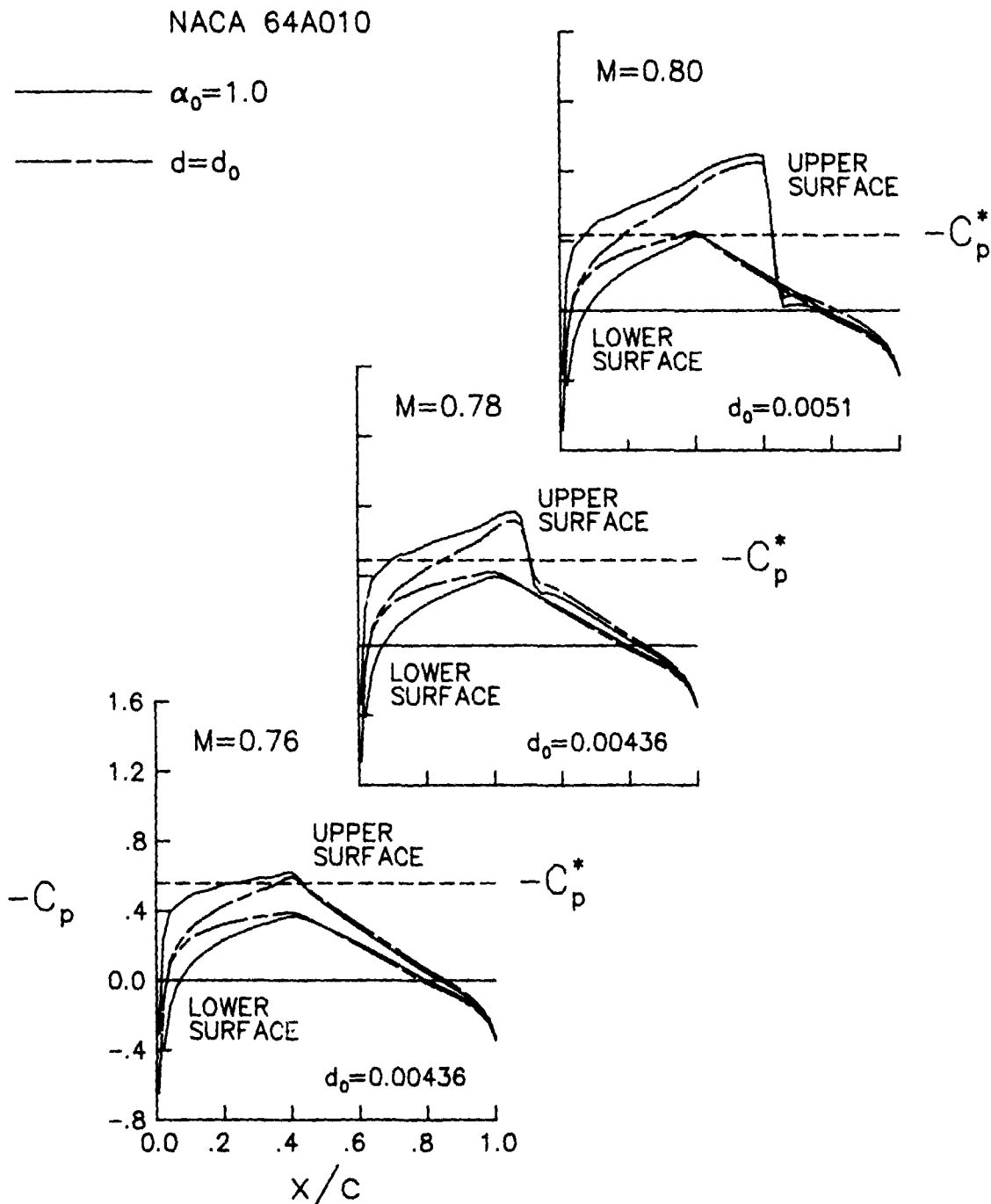
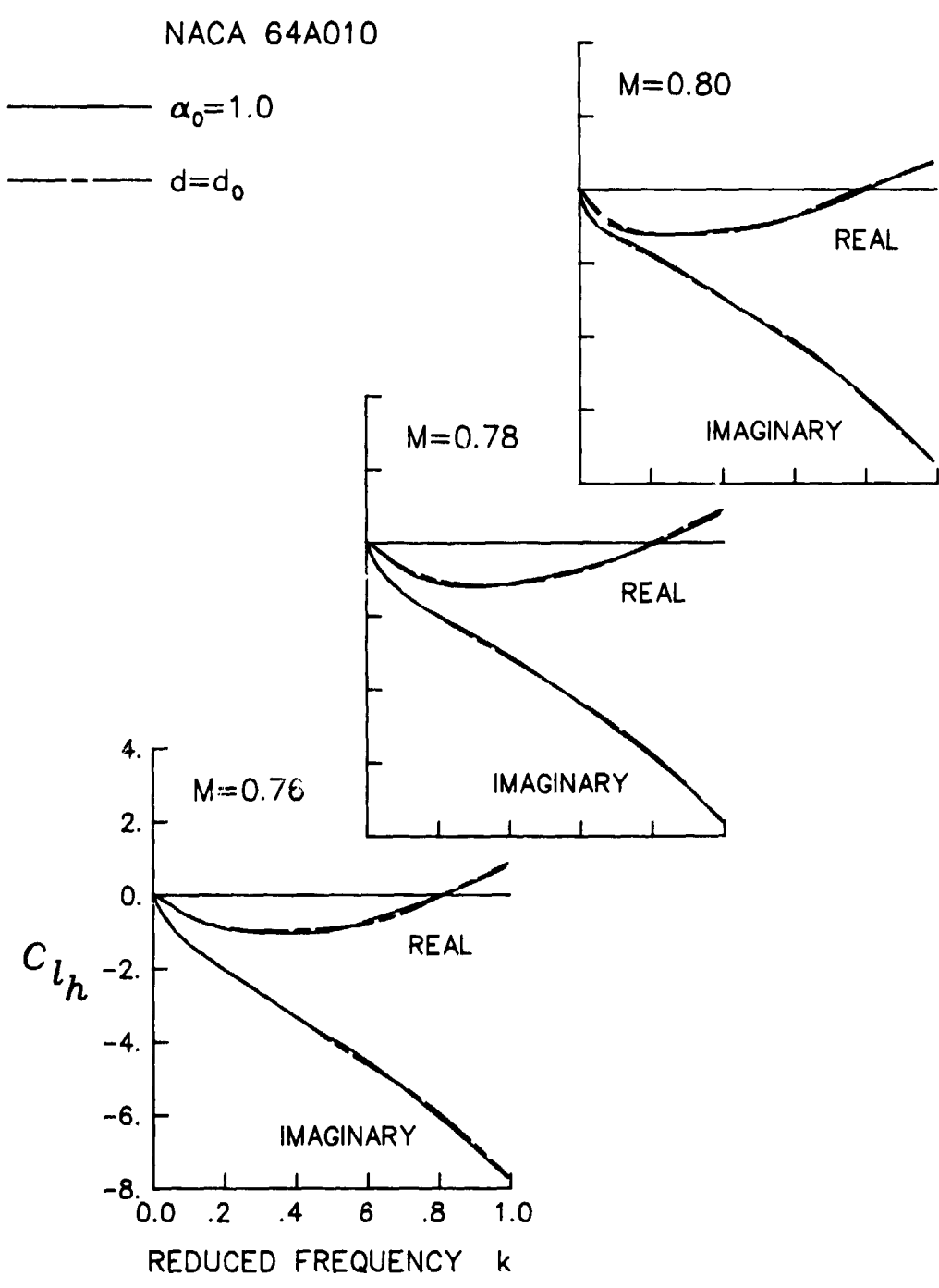
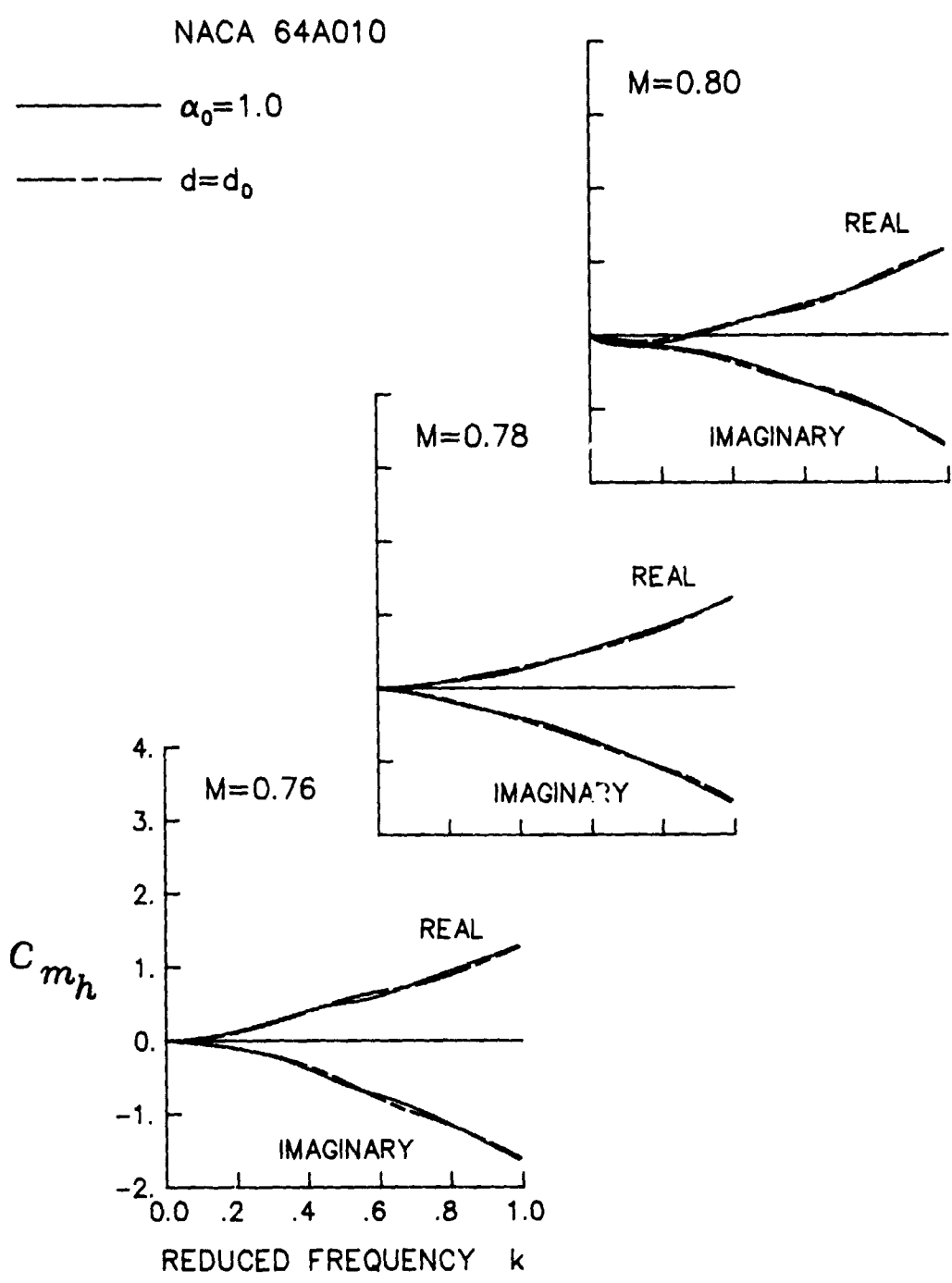


Figure 12. Comparison of aerodynamic parameters for NACA 64A010 airfoil with $\alpha_0 = 1.0^\circ$ or $d = d_0$.



(b) Lift coefficient due to plunge.

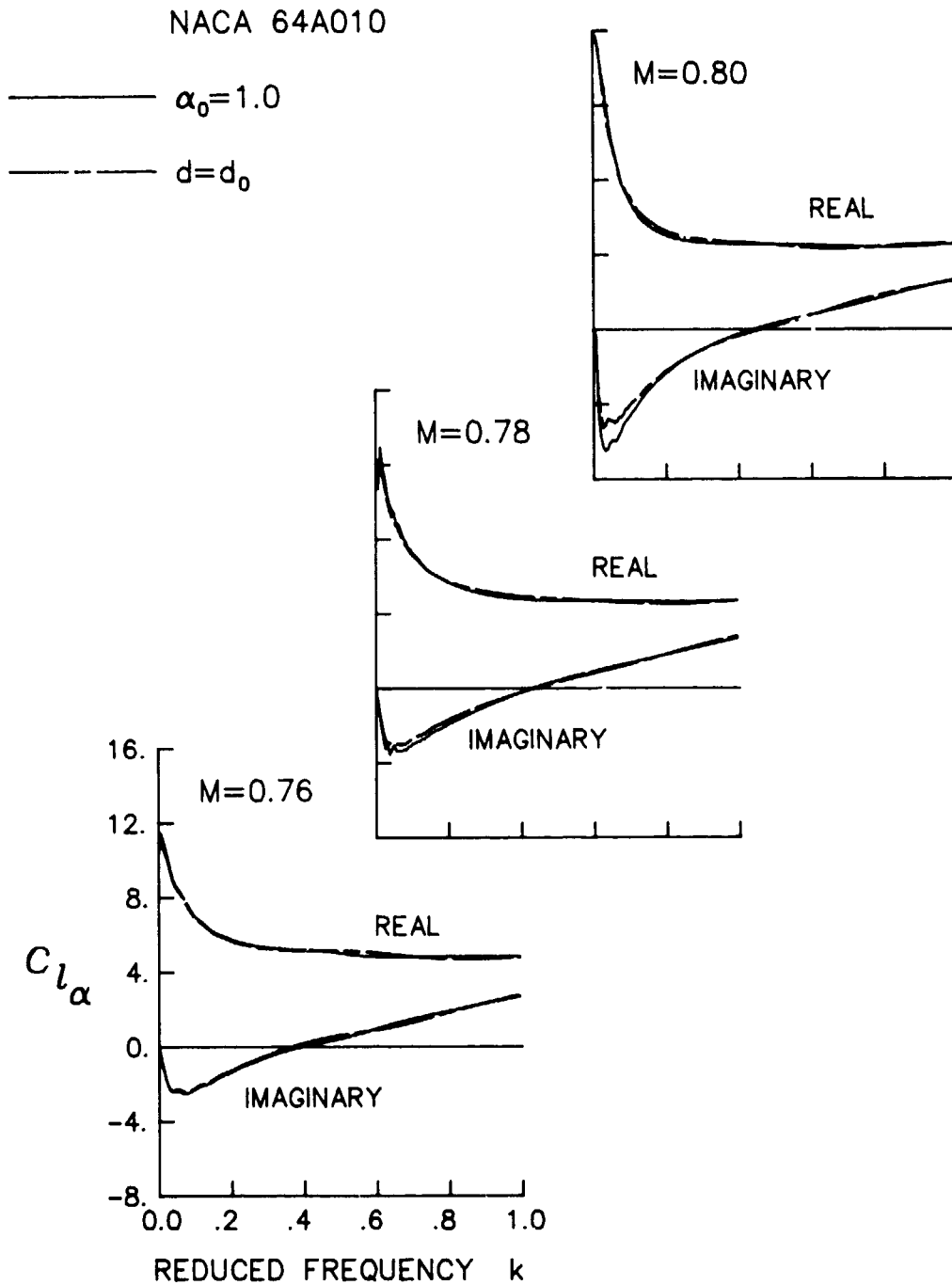
Figure 12. Continued.



(c) Pitching-moment coefficient due to plunge.

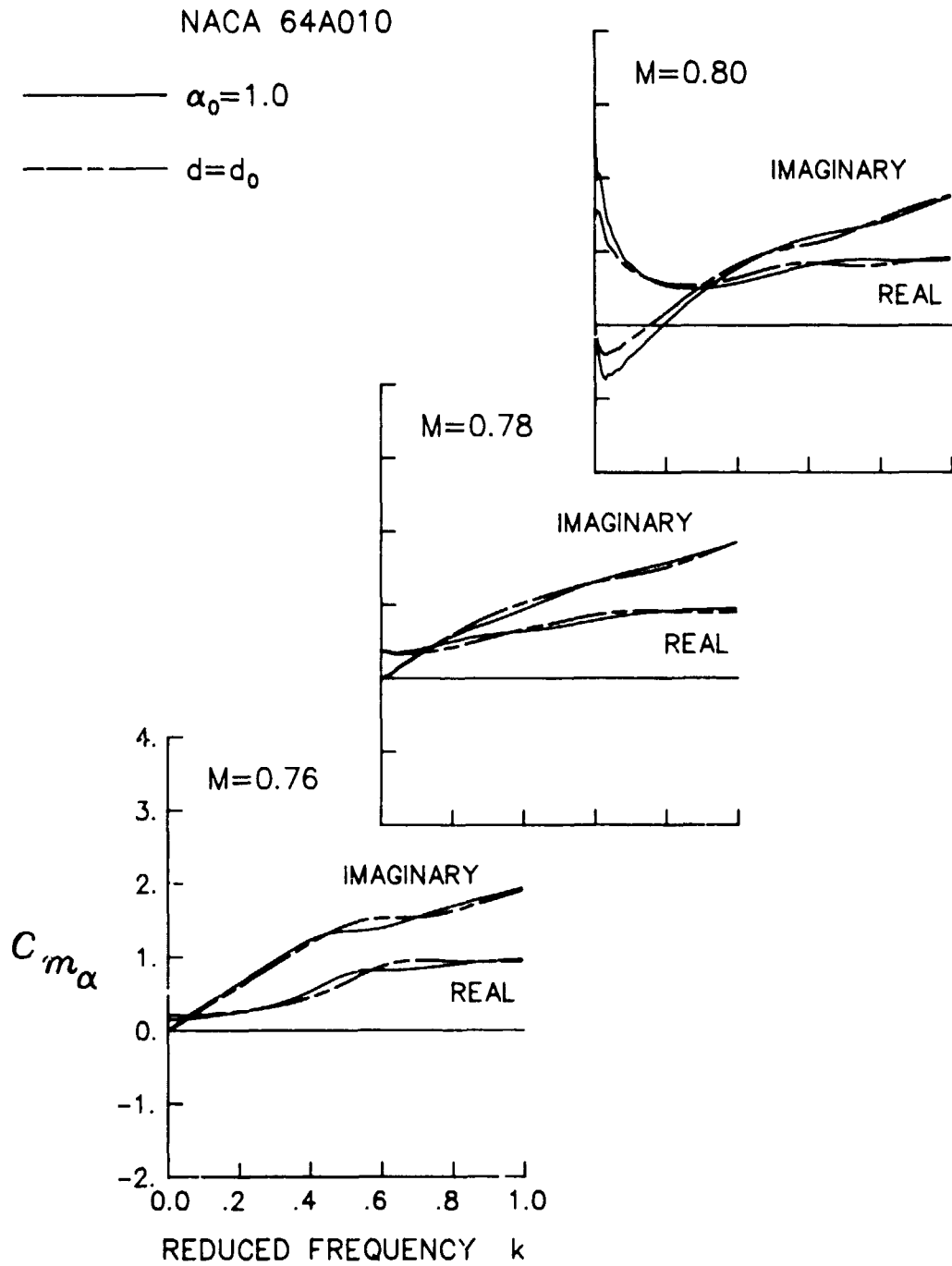
Figure 12. Continued.





(d) Lift coefficient due to pitch.

Figure 12. Continued.



(e) Pitching-moment coefficient due to pitch.

Figure 12. Concluded.

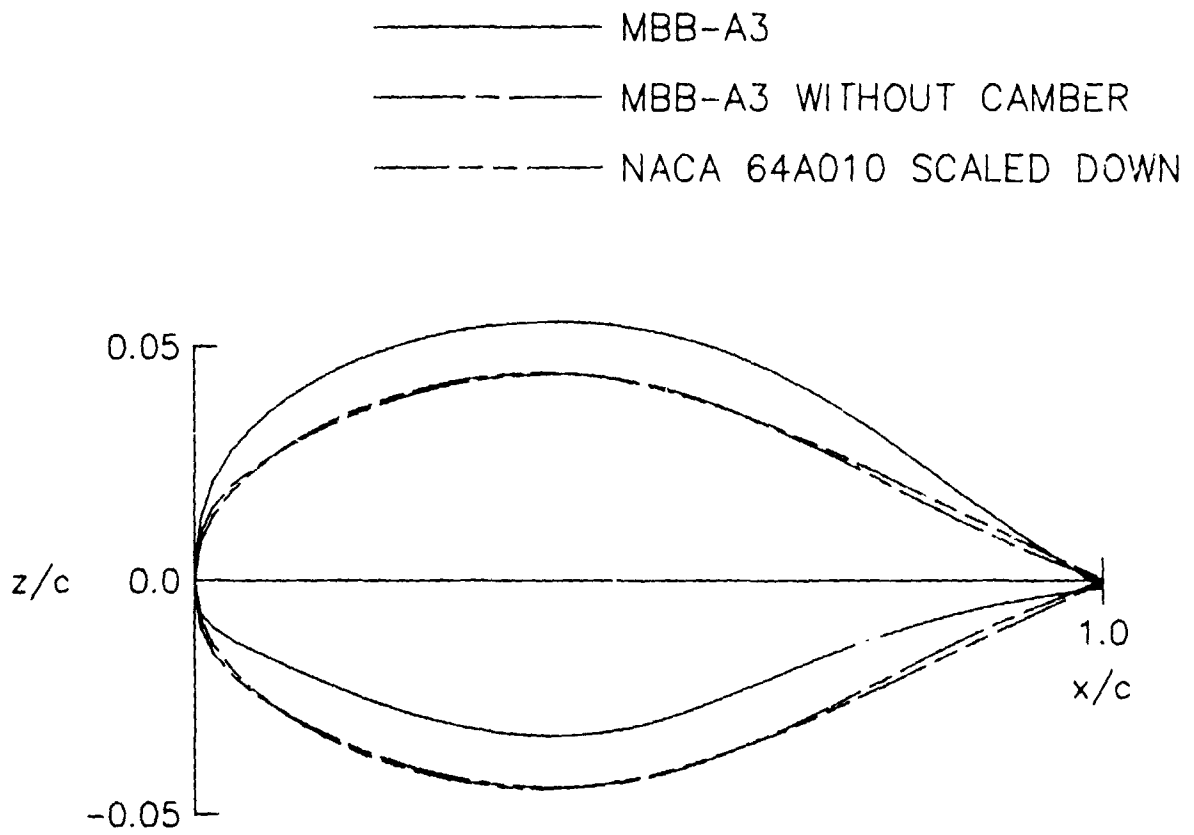


Figure 13. Comparison of airfoil profiles of MBB-A3, MBB-A3 without camber, and scaled down NACA 64A010.